Investigation of mesospheric and thermospheric emission signals from SCIAMACHY limb and nadir measurements

Final report 2007

Marco Scharringhausen, Holger Winkler, John P. Burrows, and Miriam Sinnhuber
Institute of Environmental Physics, University of Bremen,
Otto-Hahn-Allee 1, 28359 Bremen, Germany

Arthur C. Aikin
The Catholic University of America, Washington, DC 20064, U.S.A.

December 18, 2007

Contents

1 Introduction **5**
1.1 Origin and role of metal species in the upper atmosphere 5

2 Chemistry of Mg and Mg^+ **6**

3 A 2D retrieval scheme for SCIAMACHY limb and nadir data **11**
3.1 Retrieval principle 11
3.2 Obtaining column densities 13
3.3 Choice of the retrieval pixel grid 15
3.4 Calculation of optical depths $e^{-\tau_{ij}}$ and geometrical paths s_{ij} . . 18
3.5 Regularization 20
3.6 Retrieval errors and resolution 20
3.7 Systematic errors 22
3.8 Comparison with other measurements and model calculations . . 24

4 Review of the complete SCIAMACHY data set **26**
4.1 Observations 26
4.2 Discussion 35
4.3 Mg / Mg^+ measurements in the lower thermosphere 39

5 Correlation with solar activity **41**
5.1 Correlation with proton fluxes 43
5.2 Correlation with the 10.7 cm radio flux 45
5.3 Vertical profiles and 10.7 cm radio flux 45
5.4 Conclusions 46

6 Solar proton events and upper atmosphere magnesium **47**
6.1 Observations 48
6.2 Discussion 60

7 Magnesium species and meteor activity **61**
7.1 Observations 63
7.2 Conclusions 63

8 Estimation of the total influx of cosmic dust from total content and loss rates of Mg **65**

Abstract

The scope of this study is the investigation of mesospheric and thermospheric metallic species, in particular Mg and Mg^+. The methodology used in this work provides results in the mesosphere/lower thermosphere region (MLT) extending from approximately 70 to 500 km altitude.

The major source of metal species in the upper atmosphere is influx from cosmic dust. Along with Earth, a variety of celestial bodies orbit the Sun. The asteroid belt between Earth and Mars and the Kuiper belt outside the orbit of Neptune are well-known regions of high abundance of those objects. In addition, a number of regularly returning cometary objects present sources of cosmic material. The origin of these comets is believed to be the Oort cloud surrounding the solar system. After entering the atmosphere, particles from either source are then subject to frictional heating. This leads to sublimation of metallic species from the surface of the particles.

The impact of metal species on the chemistry and physics of the upper and middle (and, eventually, the lower) atmosphere is still a field of intense research. The total influx of meteoric cosmic material into the atmosphere is highly uncertain. Metal species are suggested to impact the removal of ozone in the upper stratosphere and the formation of water vapor in the mesosphere. Additionally, the role of meteoric particles in the formation of stratospheric clouds is of scientific interest.

In the first two sections of this report, an introduction is given to the physical and chemical processes which control the abundance of Mg and Mg^+ in the MLT.

Space-borne measurements present the most powerful method to investigate global distributions of metal species with moderate vertical and horizontal resolution. The SCIAMACHY instrument has the capability to observe emission signals from mesospheric and thermospheric magnesium species on a global scale with good spatial and temporal coverage.

Atmospheric profiles of Mg^+ and Mg have been derived from the SCIAMACHY data sets by the means of a tomographic retrieval scheme which simultaneously uses limb and nadir data. A description of the retrieval principle, including an error estimation, is presented in Section 3.

In Section 4 a review is given of the complete retrieval results for Mg^+ and Mg considering both total columns as well as profiles. The results represent the first vertically resolved satellite measurements of mesospheric magnesium species on a global scale, and a long period of time based on the first six years of measurement (2002 – 2007) of the SCIAMACHY instrument. A comprehensive review of the distribution and variability of the two major atomic mesospheric magnesium species (Mg and Mg^+) in the upper mesosphere and lower thermosphere is provided. Seasonal variations are investigated. In the northern hemisphere, pronounced seasonal variation with summer maxima has been found for the ionized species Mg^+. The neutral species does not exhibit such variation. At the end of Section 4, preliminary results from a new SCIAMACHY limb scanning mode which includes the lower thermosphere are presented.

The correlation between the abundance of magnesium species and the solar activity is investigated in Section 5. This includes a general long-term consideration over all six years of measurement as well as short-term observations made during a large outburst of solar particles in October and November 2003. No impact of variations in the solar activity on the total content of either Mg^+ or Mg has been observed. On the other hand, during the October/November 2003 period of high solar particle

flux, strong enhancements in both magnesium species have been observed. This is addressed in Section 6.

A long-term study has been carried out to analyze the impact of meteor showers on the total content of magnesium species in the upper atmosphere. The impact of meteoric showers on the total content has been found to be below the detection limit (Section 7). It can thus be concluded that the additional mass influx of meteor showers is negligible compared to the average background flux.

Finally, in Section 8, an estimation of the total influx of meteoric material is made from the total content of Mg, and first-order chemical loss rates. It is estimated that a total amount of approximately 55 t enters the atmosphere per day.

While generally, the atmospheric Mg and Mg^+ contents measured by SCIAMACHY are in the range expected from atmospheric models and comparable to previous measurements, the investigation of the SCIAMACHY data set has provided a number of unexpected results that need to be investigated further; the large impact of the Oct 2003 solar proton event on both metal and metal ion, the upward drift of Mg^+ in the auroral regions, or the observation of a Mg^+ / Mg layer between 150 - 200 km altitude.

1 Introduction

1.1 Origin and role of metal species in the upper atmosphere

The scope of this study is the investigation of mesospheric and thermospheric metallic species. The methodology used in this work provides results in the mesosphere/lower thermosphere region (MLT) extending from approximately 70 to 500 km altitude. This region forms the boundary between the atmosphere and space and is subject to a number of energy inputs in the form of solar wind particles and electromagnetic radiation. Gravity waves, tides and planetary waves present energy influx from lower altitudes.

The major source of metal species in the upper atmosphere is influx from cosmic dust. Along with Earth, a variety of celestial bodies orbit the Sun. The asteroid belt between Earth and Mars and the Kuiper belt outside the orbit of Neptune are well-known regions of high abundance of those objects. As a result of perturbations by gravitational forces, small particles of micrometer sizes as well as larger objects of sizes up to several meters leave their natural orbits and enter the Earth's gravitational field. In addition, a number of regularly returning cometary objects present sources of cosmic material. The origin of these comets is believed to be the Oort cloud surrounding the solar system. The radius of this cloud is estimated to be several thousand astronomical units. While approaching the Sun, the cometary material is evaporating and sublimating from the comets, forming trails that can often be observed by eye from the ground. Passes of the Earth through these trails result in material influx into the atmosphere [Goldberg and Aikin, 1973].

After entering the atmosphere, particles from either source are then subject to frictional heating. This leads to sublimation of metallic species from the surface of the particles.

The impact of metal species on the chemistry and physics of the upper and middle (and, eventually, the lower) atmosphere is still a field of intense research. Estimations for the total influx of cosmic material differ by more than one order of magnitude, ranging from 20 to 400 t/d ([Hughes, 1978], [McBride and McDonnell, 1999], [Cziczo et al., 2001], [Wasson and Kyte, 1987]). Beside postulations with respect to chlorine catalyzed removal of ozone in the upper stratosphere [Murad et al., 1981], the formation and role of so-called *meteoric smoke* is highly uncertain. Meteoric smoke is a result of polymerization of metal compounds and silicon oxides [Kalashnikova, 2000]. Heterogeneous chemistry on the surface of these particles may then lead to formation of water vapor at altitudes of approximately 70 km [Summers and Siskind, 1999].

Murphy et al. [1998] propose that metal-rich particles such as meteoric smoke particles may act as condensation nuclei for stratospheric clouds. Figure 1 gives a visual review of the origin and the role of metal species in the upper and middle atmosphere.

A somewhat inverse question is that of the interaction of meteoric metals with cloud particles in the mesosphere. In the summer mesopause region at altitudes between 82 and 87 km *Polar Mesospheric Clouds* (also termed *Noctilucent Clouds*, NLCs) form from ice particles during periods of very low temperatures around 150 K. It has been proposed that metal species are taken up on the surface of the ice particles and thus removed from the gas phase. Lidar mea-

surements of iron profiles in the South Pole region [Hunten, 2004] are consistent with model calculations done by Plane et al. [2004]. Lidar measurements carried out in Spitsbergen, Norway, reported a similar behavior for potassium [Lübken and Höfner, 2004].

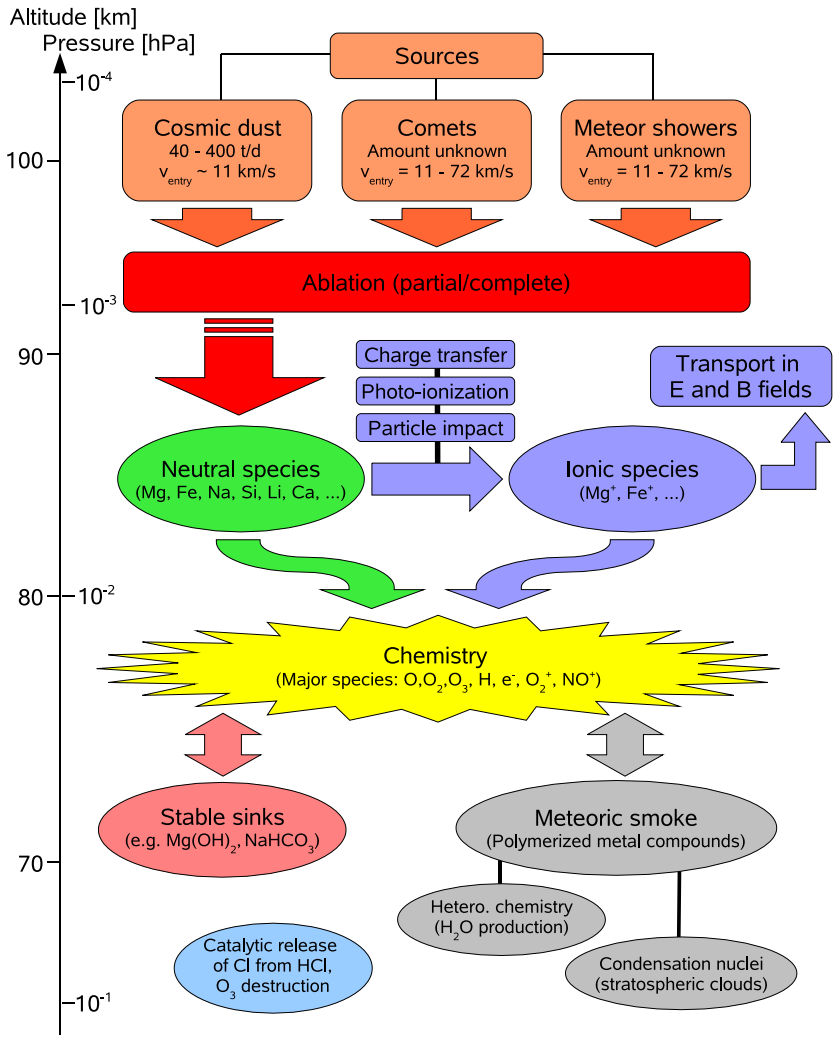

Figure 1: Review of major processes for metal species in the upper atmosphere. Major questions arising are the total influx of cosmic material and the role of metal compounds for the physics and chemistry of the middle and lower atmosphere.

2 Chemistry of Mg and Mg^+

Though the ionized species Mg^+ has been measured occasionally by rocket-borne ion mass spectrometry, very little is known about the abundances of the neutral atom. This is mainly due to the fact that ground-based measurement

techniques (lidar, photometry) using the Mg fundamental emission at 285 nm are impossible due to the strong ozone absorption in the Hartley bands at these wavelengths.

Intense laboratory studies as well as model simulations have been undertaken to estimate loss and production processes at respective altitudes; results are reported in Plane and Helmer [1995], Plane [2003], Fritzenwallner and Kopp [1998])

The dominant ionic species at altitudes above 150 km, i.e. within the F-region, are atomic species like ionized oxygen and nitrogen. At lower altitudes within the D- and E-region (60 – 80 km and 80 – 150, respectively), molecular species O_2^+ and N_2^+ become more abundant and thus important for the chemistry.

A number of strong ionization processes leads to high concentrations of ionic species at altitudes above 60 km. The major source of ionization of neutral magnesium is charge transfer. Beside this, ionization is possible by solar UV radiation, particle impact (a source of increased importance in the auroral regions near the geomagnetic poles), and cosmic rays. However, the impact of cosmic radiation is weak and will be neglected in the discussion of the metallic chemistry.

A thorough overview of the chemistry of mesospheric and thermospheric magnesium is given in Plane and Helmer [1995]. See Figure (4) for an overview of the chemistry of mesospheric and thermospheric magnesium. Figure 2 presents vertical profiles of major magnesium species in the altitude range from 65 to 110 km for mid-winter, mid-latitude daylight conditions.

According to the work presented in Plane and Helmer [1995], the prevailing source reactions of ionized magnesium Mg^+ in the mesosphere are:

$$\begin{aligned} Mg + NO^+ &\rightarrow Mg^+ + NO && (1)\\ Mg + O_2^+ &\rightarrow Mg^+ + O_2 && (2)\\ Mg + h\nu(\leq 162.2\text{nm}) &\rightarrow Mg^+ && (3) \end{aligned}$$

Middle UV radiation as in the Lyman-α emission around 121 nm, penetrates easily down to lower atmospheric levels of 70 – 80 km, depending on solar zenith angle, leading to photo-ionization of Mg. At altitudes above approximately 80 km, the dominant ionization process to form Mg^+ is charge transfer with one of the dominant molecular species (compare Figure (3)).

Dominant loss reactions of singly ionized magnesium to form neutral Mg are radiative recombination (reaction (4)) and dissociative recombination (reactions (8), (9)) after preceding formation of molecular ions (reactions and (5), (6)). Note that the formation of molecular ions is possible via reaction of the neutral species Mg and following ionization as well.

$$\begin{aligned} Mg^+ + e^- &\rightarrow Mg + h\nu && (4)\\ Mg^+ + O_3 &\rightarrow MgO^+ + O_2 && (5)\\ Mg^+ + O_2 + N_2 &\rightarrow MgO_2^+ + N_2 && (6)\\ MgO^+ + O &\rightarrow Mg^+ + O_2 && (7)\\ MgO^+ + e^- &\rightarrow Mg + O && (8)\\ MgO_2^+ + e^- &\rightarrow Mg + O_2 && (9) \end{aligned}$$

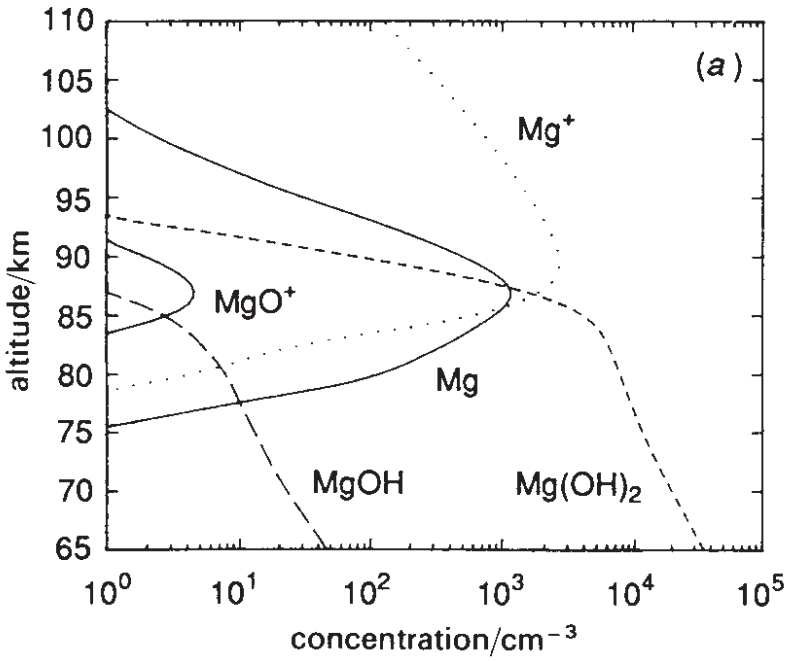

Figure 2: Vertical profiles of the major magnesium species in the mesosphere and lower thermosphere for a mid-latitude winter daylight scenario (adapted from Plane and Helmer [1995]). The major reservoir species at lower altitudes is $Mg(OH)_2$. The Mg profiles exhibits a maximum number density at approximately 87 km whereas the Mg^+ peak abundance is slightly higher up in the atmosphere at approximately 90 km.

At high altitudes, however, the regeneration of Mg^+ by reaction with atomic oxygen (7) is very fast. Thus, the radiative recombination (4) is the dominant pathway at high altitudes. As a result of the fact that this reaction itself is very inefficient, the lifetime of ionized Mg is quite long at high atmospheric levels.

At lower altitudes, major species for reaction with metal species are O, O_2, O_3, H, H_2 and H_2O. Magnesium will form stable oxides or hydroxides as their dominant compounds [Plane, 2003].

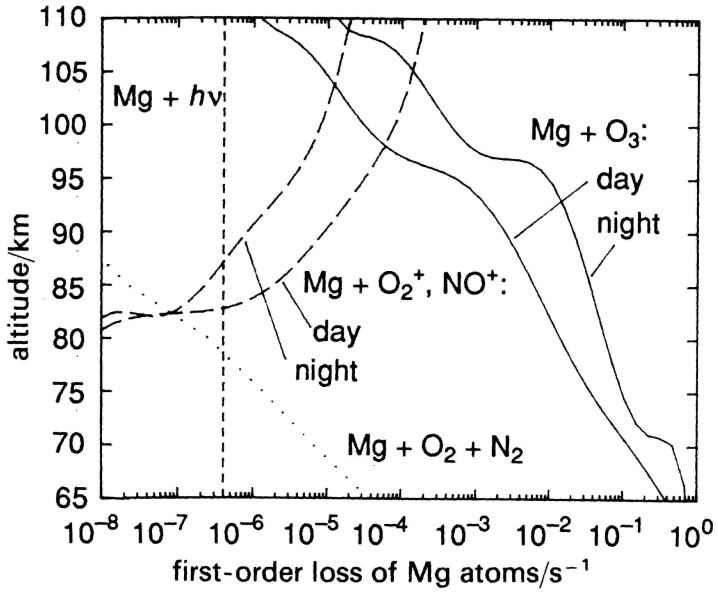

Figure 3: Loss rates in the Earth's atmosphere (north mid-latitude winter scenario) for neutral Mg (adapted from Plane and Helmer [1995]). At high altitudes, charge transfer with molecular oxygen and nitrogen ions is the most efficient loss reaction. Lower down in the atmosphere, the major loss reaction is presented by reaction with ozone to form the magnesium oxide MgO. This is then converted to its stable reservoir $Mg(OH)_2$ by reaction with water vapor, see reaction (11).

The major stable sink species of magnesium species is $Mg(OH)_2$, it is formed by reaction of magnesium oxide with water molecules:

$$\mathrm{Mg} + \mathrm{O_3} \rightarrow \mathrm{MgO} + \mathrm{O_2} \tag{10}$$

$$\mathrm{MgO} + \mathrm{H_2O} + \mathrm{M} \rightarrow \mathrm{Mg(OH)_2} + \mathrm{M(M = O_2, N_2)} \tag{11}$$

See Figure 2 for a vertical profiles of the major sink species. According to Plane and Helmer [1995], possible reservoir species like MgO_3 and $MgCO_3$ are expected to spontaneously decompose, as the reactions (12) and (13) are highly endothermic.

$$MgO_3 + O \rightarrow MgO_2 + O_2 \quad (12)$$
$$MgCO_3 + O \rightarrow MgO_2 + CO_2 \quad (13)$$

Neutral Mg is recovered by double hydrogenolysis of the reservoir species ((14), (15)). This reaction depends on the abundance of atomic hydrogen and is thus most efficient under daylight summer conditions.

$$Mg(OH)_2 + H \rightarrow MgOH + H_2O \quad (14)$$
$$MgOH + H \rightarrow Mg + H_2O \quad (15)$$

A schematic sketch of the magnesium chemistry in the upper atmosphere is presented in Figure 4. It should be noted that for less than half of the major reaction pathways, reaction coefficients have actually been measured in the laboratory. The remaining coefficients had to be estimated or calculated from quantummechanical principles. The reliability of model results in general suffers from these uncertainties.

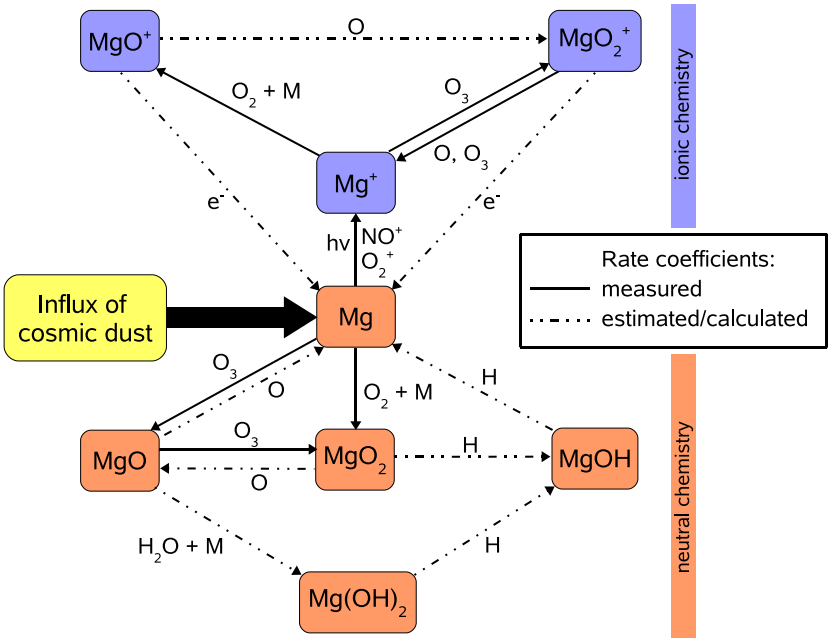

Figure 4: Overview of the chemistry of Mg, Mg^+ and respective compounds in the upper atmosphere. Adapted from Plane and Helmer [1995], solid lines indicate reactions for which corresponding rate coefficients have been measured.

3 A 2D retrieval scheme for SCIAMACHY limb and nadir data

A comprehensive retrieval scheme for SCIAMACHY limb and nadir measurements is presented in this section. The next two sections are dedicated to the description of a two-dimensional retrieval scheme designed to overcome this problems and allow SCIAMACHY to obtain altitude information above the top tangent altitude. The retrieval simultaneously uses all limb and nadir measurements of one orbit. A discussion of the instrumental error is contained in Section 3.7.

3.1 Retrieval principle

Figure 5 shows a typical orbit measurement sequence of SCIAMACHY. As can be seen from the figure, a number of air volumes is traversed by several lines-of-sight (LOS) in limb as well as in nadir geometry. This circumstance can be used to overcome the drawbacks of integration over a long part on the LOS. A number of SCIAMACHY measurements are evaluated simultaneously.

The retrieval presented in the following is based on the fundamental assumption that the atmosphere is in steady-state during the duration of one orbit. This assumption is reasonable, as the day lit part of a single orbit is completed in approximately 50 minutes.

For a single orbit, a fixed partition of the atmosphere in $nPix$ pixel is assumed. A detailed description of the pixel grid is given in Section 3.3. Let x_i be the number density within the i-th pixel. It is assumed to be constant within the pixel. As the emitted radiation is proportional to the number density within the i-th pixel as well as to the pathlength s_{ij} of the LOS no. j within the pixel, the contribution of a single pixel is given by

$$I_j(\lambda) = x_i \cdot \gamma_{ij}(\lambda) \cdot s_{ij} \cdot \exp\left(-\tau_{ij}(\lambda)\right) \cdot F(\lambda). \tag{16}$$

Obviously the factors s_{ij} are non-zero only for those pixels being traversed by the LOS no. j (see Section 3.3). In equation (16) $F(\lambda)$ denotes the solar irradiance at the top-of-atmosphere (TOA) at wavelength λ. The emissivity factors γ_{ij} are explained and derived in Section 3.2. These present proportionality factors between the observed radiance and the number densities. The quantity $\exp\left(-\tau_{ij}(\lambda)\right)$ denotes the extinction along the LOS from the pixel to the instrument as well as the extinction from the Sun to the pixel along the line-from-the-Sun (LFS). Obviously, this quantity depends on wavelength. Within the mesosphere and thermosphere, extinction in the wavelength range of 200 – 300 nm is mainly a result of absorption within the ozone Hartley-Huggins bands and Rayleigh scattering out of the LOS respectively LFS. See Section 3.4 for a detailed description of the calculation of the τ values.

The total observed radiance for a single line-of-sight – either limb or nadir – numbered j, is then given by

$$I_j(\lambda) \approx \sum_{i=1}^{nPix} x_i \cdot \gamma_{ij}(\lambda) \cdot s_{ij} \cdot \exp\left(-\tau_{ij}(\lambda)\right) \cdot F(\lambda). \tag{17}$$

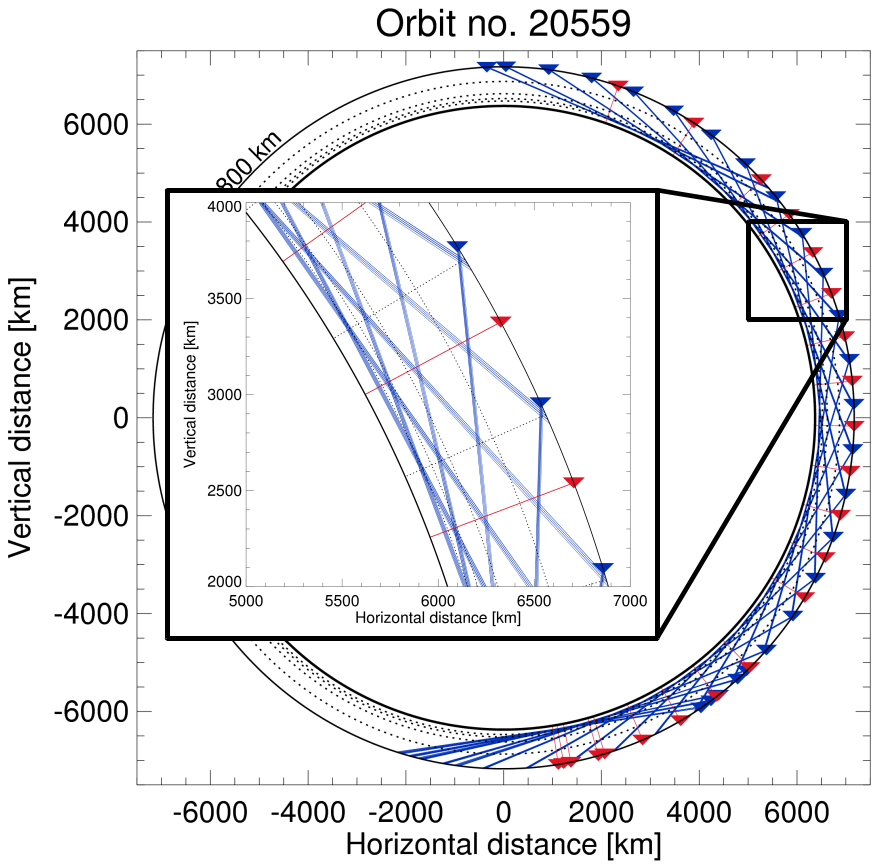

Figure 5: Typical orbit measurement sequence of SCIAMACHY. This figure is to scale. Triangles denote the satellite positions, lines-of-sight in limb geometry are drawn blue, and red lines correspond to nadir measurements. An atmospheric pixel grid representative to the one being used in the retrieval presented here is indicated partly by dotted lines. The 100, 150, 250, 500 km altitude levels are represented by dotted circles. Dotted radial lines depict the angular partitioning. In angular direction, each pixel is centered around the average tangent point of a single limb scan sequence from the surface to the top tangent altitude. The SCIAMACHY orbit sequence comprises of limb scans which are on average 7° apart, and this results in pixels of the same angular width on average. See Section 3.3 for a detailed description of the pixel grid.

Equation (17) presents a system of linear equations and can be written in a more convenient form using matrix notation. Let I denote the vector of limb and nadir measurements, ordered in an arbitrary but fixed way. Given *nLimb* limb and *nNadir* nadir measurements, obviously $I \in \mathbb{R}(nLimb + nNadir)$. The quantities x_i are combined in a vector $x \in \mathbb{R}(nPix)$. Equation (17) may be written in a more convenient matrix-vector form using the *weighting function matrix* $K \in \mathbb{R}(nLimb + nNadir, nPix)$:

$$I(\lambda) = K(\lambda) \cdot x + \varepsilon(\lambda) \quad , \quad K_{ij} = s_{ij}\gamma_{ij}(\lambda) \exp\left(-\tau_{ij}(\lambda)\right) F_i(\lambda). \tag{18}$$

The quantity ε denotes the discretization error. For convenience, the argument λ is omitted from now on. Let $nMeas = nLimb + nNadir$.

Solving equation (18) provides the desired values of the number densities x_i. In most cases, however, the matrix K is not quadratic, rank-deficient and not well-conditioned. Thus, it is not possible to solve this system of linear equations uniquely using classical ways such as Gauß elimination. In general, a multitude of solutions to the system exist, and these depend sensitively on variations of the input parameters. The inevitable presence of noise and the discretization error result in huge variations in the retrieval solution.

Instead, a certain amount of additional information about the solution has to be applied. This is accomplished using a *regularization scheme*, see Section 3.5.

3.2 Obtaining column densities

This section treats the evaluation of the I_j as given in equation (17). For simplification, the case of one emitter with number density N is explained. As a result of absorption of solar radiation, atoms as well as molecules exist in excited energy states. Excitation to electronically elevated states requires large amounts of energy, compared to excitation to vibrationally or rotationally excited states for molecules. Additionally, the life time of excited states is rather short, i.e. spontaneous de-excitation occurs typically within times to 10^{-8} s. Note that the average life time τ_j of an excited state is connected to the Einstein coefficient by $\sum_i A_{ij} = \tau_j$. For typical mesospheric temperatures of 200 K and a mean free path of the order of centimeters (as is the case for altitudes between 80 and 100 km), the mean time between collisions of individual molecules is of the order of 10^{-5} s. It is thus assumed for the retrieval presented here that collisional de-excitation via quenching with air molecules is negligible.

The observed emitted radiance I in limb and nadir is linked to the column density (vertical as well as slant) by the emissivity factor ('g-factor') γ_{ij}, which is a proportionality factor between the observed radiance (normalized by the solar irradiance) and the column density. The emissivity factor is assumed to be independent of temperature and pressure.

$$\begin{aligned} I(\lambda) &= \gamma_{ij}(\lambda) \cdot \int_{\mathrm{LOS}} F(s,\lambda) \cdot N(s)\, ds \\ &= \gamma_{ij}(\lambda) \cdot F(\lambda) \int_{\mathrm{LOS}} e^{-\int_s^{\mathrm{TOA}} \tau(s',\lambda) ds'} \cdot e^{-\int_s^{\mathrm{TOA}} \tau(s'',\lambda) ds''} \cdot N(s)\, ds \end{aligned} \tag{19}$$

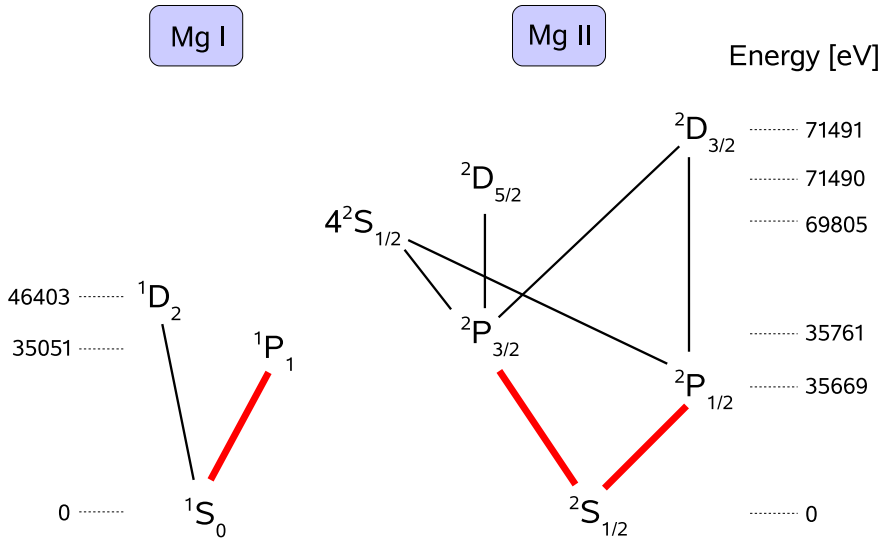

Figure 6: Grotrian diagrams of neutral Mg (Mg I) and ionized Mg^+ (Mg II). Lines connecting states of different energy denote allowed quantum mechanical transitions. Bold red lines correspond to the transitions used in the retrieval of Mg and Mg^+. These correspond to emission features at 280 and 285 nm, see Table 1 for significant parameters corresponding to the transitions depicted above.

Species	State i (lower)	State j (upper)	λ_{ij} [nm]	$A_{ij}[10^8 s^{-1}]$	$f_{ij}[-]$
Mg^+ (*)	$^2S_{1/2}$	$^2P_{1/2}$	279.553	2.60	0.61
Mg^+ (*)	$^2S_{1/2}$	$^2P_{3/2}$	280.270	2.60	0.31
Mg^+	$^2P_{1/2}$	$4^2S_{1/2}$	292.863	1.2	0.15
Mg^+	$^2P_{1/2}$	$^2D_{3/2}$	279.078	4.0	0.93
Mg^+	$^2P_{3/2}$	$4^2S_{1/2}$	293.651	2.3	0.15
Mg^+	$^2P_{3/2}$	$^2D_{3/2}$	279.793	0.79	0.093
Mg^+	$^2P_{3/2}$	$^2D_{5/2}$	279.800	4.8	0.85
Mg	$^1S_0$	$^1D_2$	215.435	$1.64 \cdot 10^{-5}$	N/A
Mg (*)	$^1S_0$	$^1P_1$	280.213	4.91	1.80

Table 1: Spectral data for Mg species. See Figure 6 for a sketch of the corresponding Grotrian diagram. This table contains the transition wavelengths λ_{ij} between two states i and j, the Einstein coefficients A_{ij} and the oscillator strengths f_{ij}. Transitions marked with (*) are between the ground state and the first excited state. Those are used for the retrieval of Mg and Mg^+ number densities. Values were obtained from NIST [2005].

Here, integration along the LOS is simply integration over altitude for nadir scans. This equation is the continuous form of equation (17). The two exponential terms in equation (19) represent the extinction along the line-from-the-Sun and the line-of-sight, respectively. See Section 3.4 for a detailed discussion of the radiative transfer used in the retrieval.

Note that I denotes the net emission, that is, the total observed radiance with the Rayleigh background removed. The calculated emissivity is convolved to the SCIAMACHY wavelength grid and then fitted using a least square fit procedure to the measured spectrum. The fit factor then constitutes the column density. In Figure 7 a visual representation of this approach is given.

The g-factor is calculated as the product of the actinic flux, the absorption cross section σ_{ij}, the relative Einstein coefficient of spontaneous emission [Anderson and Barth, 1971] and a phase function term depending on the scattering angle θ. See Scharringhausen [2007] for a detailed description of the phase function $P(\theta)$ for resonant line scattering. Here, σ_{ij} depends on the classical electron radius as well as on the transition wavelength λ_{ij} and the oscillator strength f_{ij}. The relative Einstein coefficient presents the probability of relaxation from the excited state j to the lower state i. Note that there may be a number of lower states reachable from state j. This is accounted for by normalizing A_{ij} by the sum of all respective absolute Einstein coefficients. See Figure 6 and Table 1 for a review of some transitions of Mg and Mg^+.

$$\gamma_{ij} = P(\theta) \cdot \pi F(\lambda_{ij}) \cdot \sigma_{ij} \cdot \frac{A_{ij}}{\sum_{i'} A_{i'j}} \tag{20}$$

$$= \underbrace{P(\theta)}_{\text{Phase function}} \cdot \underbrace{\pi F(\lambda_{ij})}_{\text{actinic flux}} \cdot \underbrace{\frac{\pi e^2}{mc^2} f_{ij} \lambda_{ij}^2}_{\text{abs. cross section}} \cdot \underbrace{\frac{A_{ij}}{\sum_k A_{kj}}}_{\text{rel. Einstein coeff.}} \tag{21}$$

All values necessary for numerical calculations are obtained from the NIST database [NIST, 2005].

3.3 Choice of the retrieval pixel grid

In principle, the retrieval pixel grid can be chosen arbitrarily. The mathematics of the retrieval do not relate the retrieval grid to the measurement grid. However, in practice it is desirable to adapt the retrieval grid to the measurements. Obviously, it is not reasonable to choose a grid with rectangular pixels in a Cartesian grid. Instead, a polar coordinate system is used, describing each pixel by a latitude and an altitude.

As can be seen from equation (17), the contribution of the number density in pixel no. i mainly depends on the path length s_{ij} of the LOS of measurement j within that pixel. Note that as a result of $\exp(-\tau_{ij}(\lambda)) \approx 1$, the quantity $F_i(\lambda)$ is near the value of the solar irradiance outside the atmosphere. It is desirable to have the values of s_{ij} as large as possible for each pixel to obtain a good sensitivity within pixel no. i. On the other hand, it is reasonable to design the pixel grid in a way to obtain similar values of s_{ij} for all pixels and measurements. Thus, the retrieval is more or less equally sensitive to all pixels. Additionally, coefficients of similar size improve the behavior and stability of the equation solving algorithm (see Golub and v. Loan [1996] and Section 3.5).

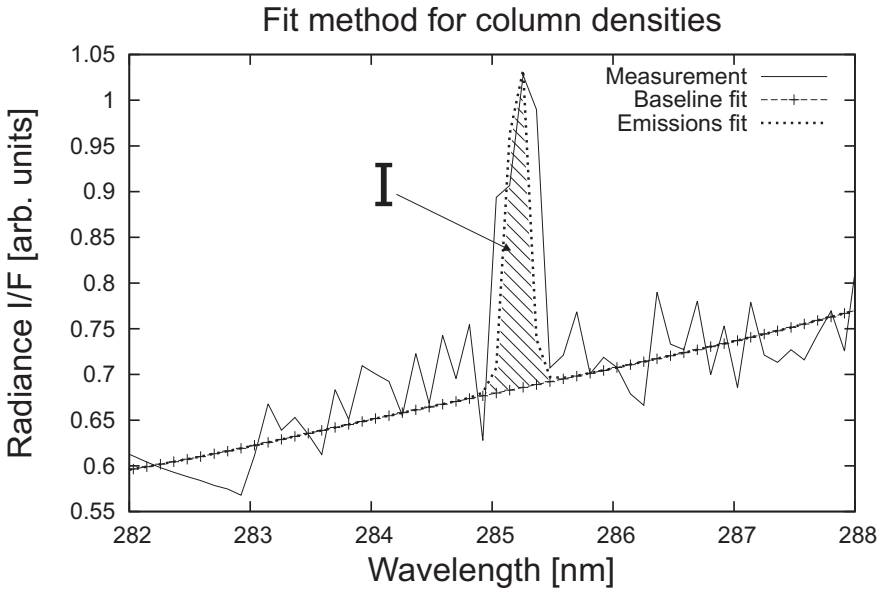

Figure 7: Sketch of the method to estimate column densities for the example of neutral Mg. The emission of neutral Mg around 285 nm observed in nadir view is shown. However, the fit method described here applies for all emissions under consideration and both measurement modes. The background is fitted using spline approximation within those wavelength ranges not containing any emission signal. In this example, the spline fit would extend from 282 to 285 nm and from 285.5 to 288 nm. The background radiance at the emission wavelengths is estimated by interpolation (spline or linear is possible, the results do not change significantly).

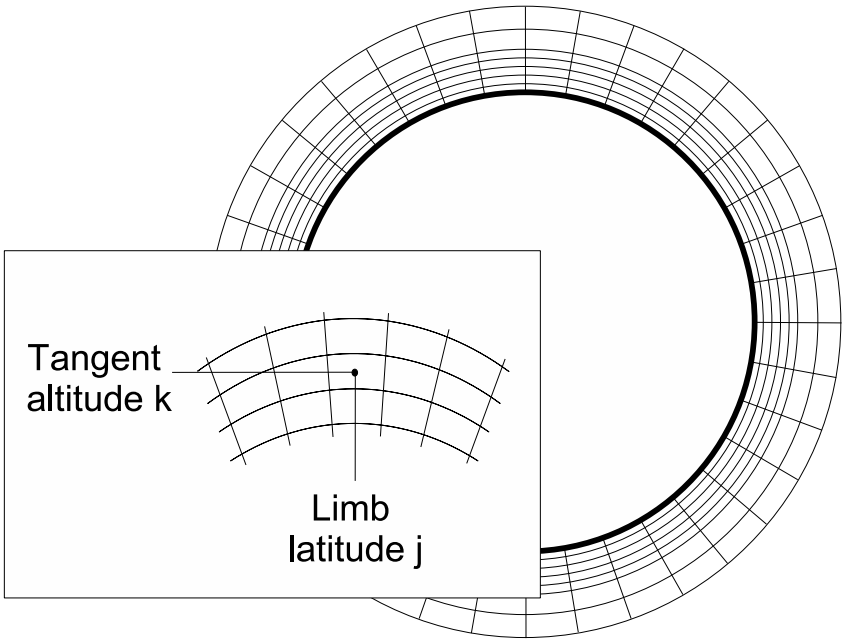

Figure 8: Outline of the retrieval pixel grid. Each latitude bin is subdivided into a number of altitude layers. Low altitude pixels are centered around limb tangent points to obtain maximum path lengths of limb lines-of-sight within the pixels. Thus, each pixel is approximately 3 km high and 7 – 15° wide. The altitude steps are increasing towards higher altitudes. This reflects SCIAMACHY's limited vertical resolution at high altitudes. See Table 2 for a quantitative description of a typical retrieval grid.

Thus, a good compromise is to define pixels centered around the limb tangent points (Fig. 8). That is, low altitude pixels have the shape

$$[\frac{1}{2}(\phi_k + \phi_{k-1}), \frac{1}{2}(\phi_k + \phi_{k+1})] \times [\frac{1}{2}(h_l + h_{l-1}), \frac{1}{2}(h_l + h_{l+1})]$$

$$\phi_i = \text{Latitude of TP no. } k \quad , \quad h_j = \text{Tangent altitude no. } l$$

Note that the retrieval uses a different pixel grid for each individual orbit. The retrieval works within the altitude range of 70 – 500 km. Low altitude pixels denote pixels within the SCIAMACHY tangent height range below 92 km. Obviously, each pixel is easily described by two numbers, namely the corresponding indices of the limb measurement. However, for purposes of the retrieval it is necessary to number all pixels from 1 to *nPix*. SCIAMACHY limb scan tangent heights do not extend into the thermosphere, thus the pixel grid has to be designed 'freely' above the top tangent altitude of ≈92 km. Retrieval tests using synthetic data (see Scharringhausen [2007]) yielded good results using four fixed altitude bins above 100 km, see Table 2. Obviously, the pixel grid cannot extend into the night side of the Earth.

A typical pixel grid is given in Table 2.

3.4 Calculation of optical depths $e^{-\tau_{ij}}$ and geometrical paths s_{ij}

At high altitudes, the solar irradiance at a certain wavelength is virtually constant and not dependent on solar zenith or azimuth angle. Similarly, absorption along the line-of-sight in either limb or nadir can be neglected. For altitudes below 85 km and wavelength less than 300 nm, however, absorption in the ozone Hartley-Huggins bands and Rayleigh scattering out of the LOS becomes significant. This is in particular the case for limb measurements, as the zenith angle of the line-of-sight is 90° . This yields long light paths. Figures 9(a) and 9(b) show limb radiances calculated by the radiative transfer model SCIARAYS [Kaiser, 2001]. One calculation is done using a pure Rayleigh atmosphere without any absorption. The limb radiance is decreasing exponentially as the simulated limb sounder proceeds to higher tangent altitudes. If absorption in the ozone bands is included, the simulated radiance differs significantly from the calculated values without ozone. Figures 9(a) and 9(b) show exemplary results for 60° solar zenith angle and 60° solar azimuth angle. The 'full atmosphere'-radiances deviate by more than 5% at altitudes below 75 km. At 70 km, the relative difference reaches 15%. Note that these deviations increase for longer light paths in the atmosphere, e.g. higher solar zenith angles.

The radiative transfer model presented here is based on a ray-tracing approach. The major advantage of this model compared to other models (see e.g. Kaiser [2001], Rozanov [2001]) is the fast computational speed and the simplicity of the source code. The model is modular and expandable for other species. This model incorporates single scattering into and out of the line-of-sight respectively the line-from-the-Sun) as well as absorption in the ozone Hartley-Huggins bands. As a result of the small density of air at mesospheric and thermospheric altitudes, refraction is negligible.

Bottom [km]	Center [km]	Top [km]
250.0	375.0	500.0
150.0	200.0	250.0
120.0	135.0	150.0
93.6	106.8	120.0
90.3	91.9	93.6
87.0	88.7	90.3
83.8	85.4	87.0
80.5	82.1	83.8
77.2	78.8	80.5
73.9	75.6	77.2
70.7	72.3	73.9

North [°]	Center [°]	South [°]
71.7	69.7	68.2
68.2	66.7	63.2
63.2	59.7	56.2
56.2	52.6	49.0
49.0	45.4	41.8
41.8	38.2	34.5
34.5	30.9	27.3
27.3	23.6	19.9
19.9	16.3	12.6
12.6	8.9	5.3
5.3	1.6	-2.1
-2.1	-5.8	-9.5
-9.5	-13.2	-16.9
-16.9	-20.6	-24.3
-24.3	-27.9	-31.6
-31.6	-35.3	-39.0
-39.0	-42.7	-46.3
-46.3	-50.0	-53.6
-53.6	-57.2	-60.8
-60.8	-64.4	-67.8
-67.8	-71.2	-74.3
-74.3	-77.4	-79.4
-79.4	-81.4	-83.4

Table 2: Typical pixel grid as used for the retrieval. In total, $11 \times 23 = 253$ pixels are defined. Figures denote the borders and center values of each pixel in altitudinal and latitudinal direction, respectively. Most pixels are approximately 3.3 km high and $7 - 15°$ wide. This holds not for the thermospheric pixels above the top tangent altitude. These values are set according to retrieval tests (see Scharringhausen [2007]). All values exemplarily shown here are derived from orbit no. 20559. Compare Figure 5 for a visualization of the orbit measurement sequence and Figure 8 for a graphical sketch of the grid.

See Scharringhausen [2007] for a thorough discussion of the calculation of optical depths and geometrical paths.

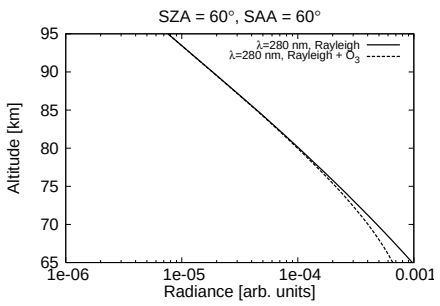

(a) Solid: Calculated for a pure Rayleigh scattering atmosphere. Dotted: Calculated including absorption in the ozone Hartley-Huggins bands.

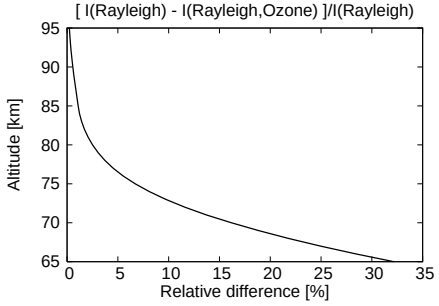

(b) Relative differences of calculations in left panel. The deviations exceed 5% at altitudes below 75 km.

Figure 9: Left panel: Limb radiances at 280 nm for different tangent altitudes and 60° solar zenith and azimuth angle, calculated for a pure Rayleigh scattering atmosphere respectively scattering and absorption in the ozone Hartley-Huggins bands. Right panel: Relative differences of limb radiances at 280 nm, calculated for a pure Rayleigh scattering atmosphere and calculated including absorption in the ozone Hartley-Huggins bands. Solar zenith angle is 60°, solar azimuth angle is 60°.

3.5 Regularization

Instead of solving (18) explicitly, it is reasonable to minimize the residual between the forward calculated state Kx and the measurement y:

$$||Kx - y||^2 \longrightarrow \min \tag{22}$$

In general, this problem does not have a unique solution. It is thus necessary to feed additional information about the true state x into the problem. However, this has to be done carefully to avoid introduction of unjustified bias. See Scharringhausen [2007] for a description of the regularization approach of this retrieval.

3.6 Retrieval errors and resolution

Similar to classical optimal estimation, averaging kernels of the functional can be calculated to investigate the information content of the measurement. By definition, the averaging kernel matrix contains the derivatives of the retrieved state $\hat{x}$ with respect to the true state x_t, i.e.

$$A = \frac{\partial \hat{x}}{\partial x_t} \tag{23}$$

Noting $y = Kx_t + \varepsilon$ (with an error vector ε), this matrix can be calculated easily (see Scharringhausen [2007]):

$$A = (K^T S_y^{-1} K + S_a + \lambda_H S_H^T S_H + \lambda_\phi S_\phi^T S_\phi)^{-1} K^T S_y^{-1} K \tag{24}$$

This derivative reflects the influence of the true state on the retrieved one. If the measurement grid is identical to the retrieval grid, an ideal measurement and retrieval would result in an unity matrix A. As a real instrument like a limb sounder has a limited spatial resolution, the retrieved number density at an altitude and a latitude may be influenced by number density at lower and higher altitudes as well as lower and higher latitudes. This is quantified by the off-diagonal elements of the rows of A. The vertical and the angular resolution can thus be estimated as the full-width-half-maximum (FWHM) of the averaging kernel functions (which are discretely represented by the rows of A).

Figures 10 and 11 show typical averaging kernel functions for the retrieval presented here. Both the altitudinal and the angular resolution of the retrieval are good. The angular resolution can be estimated from the averaging kernel functions presented in Figure 10. At all three altitudes shown, the resolution in latitude is approximately 10° . This is true for all altitudes. In comparison to the sampling of SCIAMACHY, the vertical resolution is approximately 5 km, as can be seen from Figure 11. This is a good value in comparison to the 3.3 km vertical sampling of SCIAMACHY. As SCIAMACHY limb scans do not extend into the thermosphere and the pixel sizes are larger than at lower altitudes within the mesosphere, the vertical resolution is decreased. Typical values are 25 – 35 km between 92 and 150 km, 110 km between 150 and 250 km, and 200 km between 250 and 500 km.

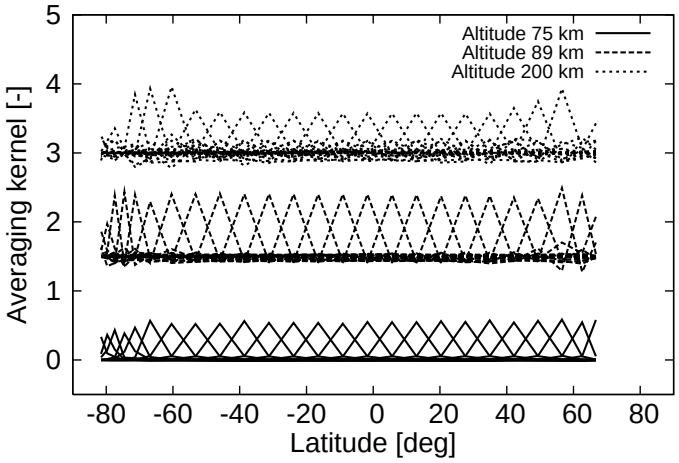

Figure 10: Averaging kernels for 75, 89 and 200 km altitude. The full-width-half-maximum is an estimate of the latitudinal resolution of the retrieval. At all three altitudes shown here, the resolution is approximately 10°. Note that the quantities shown here are $\partial \hat{x}_i / \partial (x_t)_j$ with only those components of x_t corresponding to the same altitude being considered.

The retrieval error matrix S contains the covariances of x_i with respect to x_j, for all i, j. In particular, the square roots of the diagonal elements of S present the standard deviations of the retrieval quantities x_i. This matrix is calculated as follows:

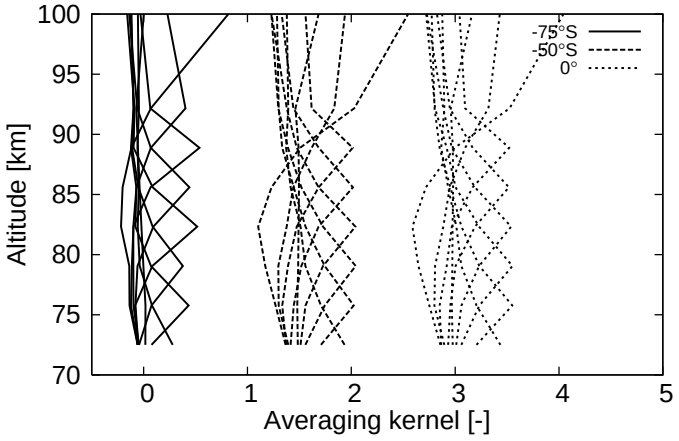

Figure 11: Averaging kernels for -75°, -50° and 0° latitude. The full-width-half-maximum is an estimate for the altitude resolution of the retrieval. At all three latitudes shown here, the resolution is approximately 5 km. Note that the quantities shown here are $\partial \hat{x}_i / \partial (x_t)_j$ with only those components of x_t corresponding to the same latitude being considered.

$$S = (K^T S_y^{-1} K + S_a + \lambda_H S_H^T S_H + \lambda_\phi S_\phi^T S_\phi)^{-1} \tag{25}$$

Figures 12 and 13 exhibit the total retrieval errors for Mg^+ and Mg for a typical orbit with good limb and nadir sampling. Note that the errors are virtually the same for both species. For the orbit used here, 23 limb scan sequences and 23 nadir scans enter the retrieval. For both species, the total error is well below 130 cm^{-3}. This a good value in comparison with the absolute values found in case studies and retrieval tests. At high altitudes, the error is slightly lower. This may be a result of the worse sampling rate at high altitudes.

3.7 Systematic errors

A number of systematic errors have to be accounted for. See Scharringhausen [2007] for a more detailed discussion of these errors.

The SCIAMACHY instrument suffers from a tangent height error of approximately 1.5 km [v. Savigny et al., 2005], [v. Savigny et al., 2006]. This pointing error is variable in space as well as in time by approximately 0.2 km. However, this variability is negligible compared to the vertical resolution of the retrieval presented here. Thus, a constant offset of 1.5 km is added to the data to correct the tangent height error.

Self-absorption of the retrieval species is negligible. This has been evaluated by theoretical considerations and retrieval test runs, see Scharringhausen [2007].

Satellite measurements of any kind are often affected by increased particle impact in the vicinity of the Southern Atlantic Anomaly, a region of anomalous high particle fluxes located eastward of South America. This region is thus excluded for most purposes.

The *Ring effect* leads to a filling up of the Fraunhofer lines in the solar spectrum if observed in scattering. This leads to errors of up to 15% in the

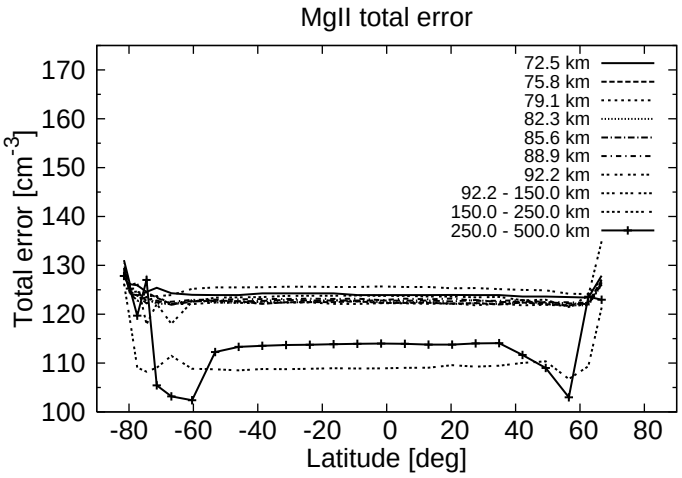

Figure 12: Total retrieval error for Mg^+, orbit no. 20559, as calculated from equation (25). For all altitudes and all latitudes, the error is below 130 cm^{-3} with a slight increase to high latitudes. This is likely a result of the decreased spatial sampling rate of SCIAMACHY. High altitudes exhibit error values of 110 – 115 cm^{-3}.

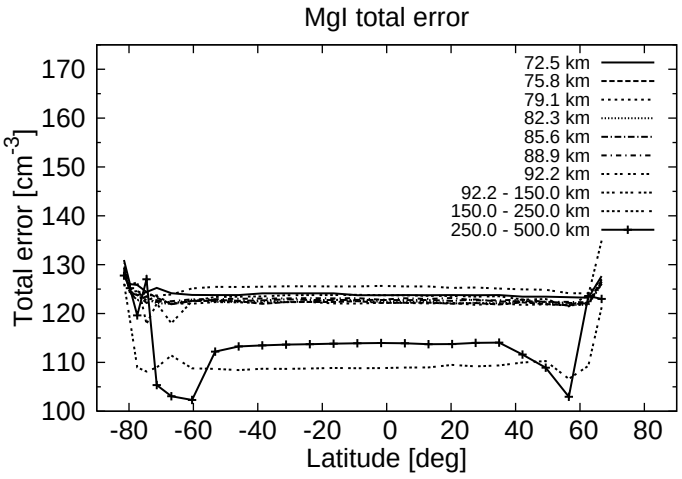

Figure 13: Total retrieval error for Mg^+, orbit no. 20559, as calculated from equation (25). For all altitudes and all latitudes, the error is below 130 cm^{-3} with a slight increase to high latitudes. This is likely a result of the decreased spatial sampling rate of SCIAMACHY. High altitudes exhibit error values of 110 – 115 cm^{-3}.

spectral data. However, the retrieval presented here does not include a Ring correction. This will be implemented in later versions.

3.8 Comparison with other measurements and model calculations

The total column values presented here show good agreement with other data (see Figure 17(a) and Section 4.1.2 for a more comprehensive review of column densities of both magnesium species, compare Table 3). Modeled total column densities are of the order of 10^7 to 10^{10} cm^{-2}, exhibiting a large variability depending on measurement and model input. The measured column densities are of the order of 10^9 – 10^{10} cm^{-2} with a large variability of approximately one order of magnitude.

Slant columns (not shown here) observed by SCIAMACHY are of the order 10^8 to 10^{10} cm^{-2}, in good agreement with previous measurements of slant column densities published by [Fesen and Hays, 1982a], [Fesen et al., 1983], [Gérard and Monfils, 1978] and [Joiner and Aikin, 1996].

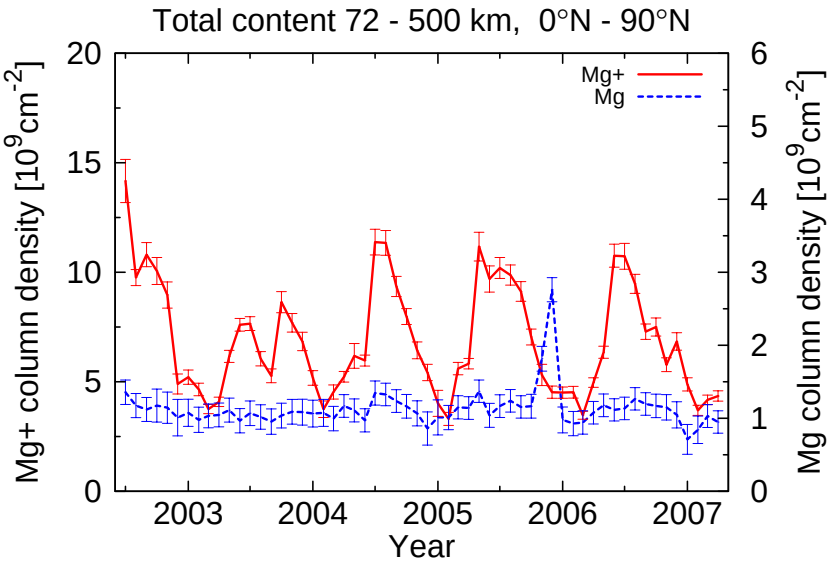

Figure 14: Total column densities of Mg^+ (solid) and Mg (dotted) for the northern hemisphere, zonally and meridionally averaged. Measured column densities of Mg^+ are between $3 \cdot 10^9$ and $1.5 \cdot 10^{10}$ cm^{-2} . The Mg total columns are of the order of 10^9 cm^{-2} . See Section 4.1.2 for a thorough discussion of this figure.

The total column comparisons presented here do not give information about the performance of the retrieval with respect to vertical profiles and latitudinally varying distributions. However, no satellite data were available that could be compared to the SCIAMACHY data set in temporal and spatial coverage. Thus, a set of synthetic data has been generated. See Scharringhausen [2007] for results of retrieval tests with respect to the reconstruction of the synthetic distributions.

Species	Total column [cm^{-2}]	Reference
Mg^+	$2.6 \cdot 10^{10}$ ($*$)	[Aikin et al., 2004]
	$8.5 \cdot 10^{9}$ (†)	[Plane and Helmer, 1995]
	$4.1 \cdot 10^{9}$ ($*$)	[Roddy et al., 2004]
	$2.4 \cdot 10^{9}$ (†)	[McNeil et al., 1998]
	$1.0 \cdot 10^{9}$ (†)	[Fritzenwallner and Kopp, 1998]
	$4.3 \cdot 10^{9}$ (†)	[Fritzenwallner and Kopp, 1998]
	$1.7 \cdot 10^{10}$ ($*$)	[Fritzenwallner and Kopp, 1998]
	$2.1 \cdot 10^{9}$ ($*$)	[Fritzenwallner and Kopp, 1998]
Mg	$7.9 \cdot 10^{9}$ ($*$)	[Aikin et al., 2004]
	$3.5 \cdot 10^{9}$ (†)	[Plane and Helmer, 1995]
	$9.9 \cdot 10^{8}$ (†)	[McNeil et al., 1998]
	$1.0 \cdot 10^{8}$ (†)	[Fritzenwallner and Kopp, 1998]
	$7.0 \cdot 10^{9}$ (†)	[Fritzenwallner and Kopp, 1998]

Table 3: Measurements ($*$) and model calculations (†) of Mg^+ and Mg total vertical column densities. Note the wide range of values and in particular the results from [Fritzenwallner and Kopp, 1998], exhibiting a variability of one order of magnitude.

4 Review of the complete SCIAMACHY data set

This chapter presents a general review of the total abundance of both magnesium species in the atmosphere. The SCIAMACHY instrument is operational since March 2002 and performs measurements on a daily basis. The data set presented here comprises observations from July 18, 2002 until April 14, 2007. All latitudes between 82° N and 82° S are covered, a global coverage is achieved within 6 days of observation. The SCIAMACHY instrument thus offers unique capabilities to study the chemistry and physics of mesospheric and lower thermospheric magnesium species on a global scale, and a long time range. In particular, four complete years, ten solstices and eleven equinoxes are contained in the data set presented here.

Seasonal and latitudinal variations of both species are discussed. Though the ablation of magnesium from cosmic dust is restricted to rather low altitudes around 100 km, the ionic species is observed at high altitudes of up to 500 km as well. Possible escape mechanisms for the ionic species from the source layer are suggested.

4.1 Observations

4.1.1 Vertical distribution

Figures 15 and 16 show yearly and globally averaged vertical profiles of Mg^+ and Mg. Note that in Figure 15, the altitude axis is drawn in logarithmic scale, whereas Figure 16 uses a linear scale and a restricted altitude range to show a detailed profile at altitudes below 120 km.

As can be seen, the Mg^+ profile (Figures 15(a) and 16(a)) exhibits a pronounced layer with maximal densities of 600 cm^{-3} between 92 and 120 km. The altitude resolution of the retrieval is worse above the top tangent altitude, see Section 3.3. Thus, the peak height of the layer cannot be localized better than to be within the altitude range of 92 – 120 km. Above 120 km, the number densities of Mg^+ are decreasing to values of approximately 75 cm^{-3} at altitudes around 400 km. Below 120 km, Mg^+ values decrease to 50 cm^{-3} around an altitudes of 80 km. At even lower altitudes, the number densities are increasing again to values of approximately 150 cm^{-3} on average (Figure 15(a)).

The neutral species Mg shows a somewhat different behavior, see Figures 15(b) and 16(b). The most striking feature is that number densities at all altitudes are lower compared to the ionic species. Similar to Mg^+, the neutral species exhibits increasing number densities below 80 km and towards lower altitudes. Maximum number densities of up to 150 cm^{-3} are observed at the lowest retrieval altitude of 70 km. A second maximum is observed around 89 km with average number densities of approximately 125 cm^{-3} (Figure 16(b)). On average, the Mg number densities are constant between 90 and 120 km, values are approximately 75 cm^{-3} in this altitude range. At higher altitudes, the Mg concentration tends to zero values.

It should be noted that the detection limit of the retrieval is approximately 120 cm^{-3} . Thus, the only features of the Mg profile that can be considered significant are the layer around 89 km and the high abundances at the lowest retrieval altitudes.

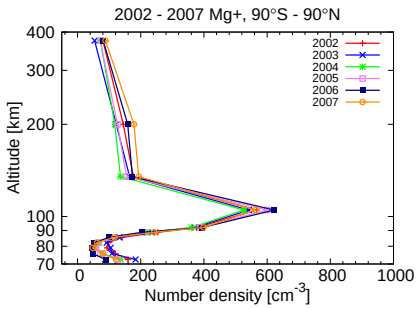

(a) Vertical profile of Mg^+, logarithmic altitude axis.

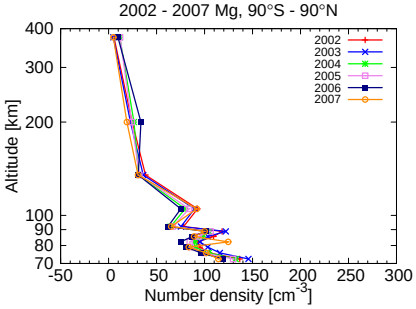

(b) Vertical profile of Mg, logarithmic altitude axis.

Figure 15: Vertical profiles of both magnesium species in the altitude range from 70 to 500 km. Note that the topmost data point corresponds to measurements between 250 and 500 km (see Section 3.3). The Mg^+ layer between 92 and 120 km with maximum number densities of 600 cm^{-3} is clearly visible. Mg^+ exhibits larger abundances in the lower thermosphere than neutral Mg. Note the different scale for the x axis. The maximal number density (125 cm^{-3}) for Mg is observed around 89 km and at the lower border of the retrieval range.

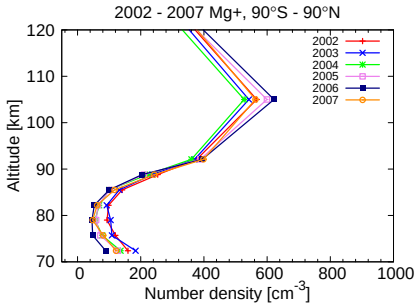

(a) Vertical profile of Mg^+ from 70 to 120 km, linear altitude axis.

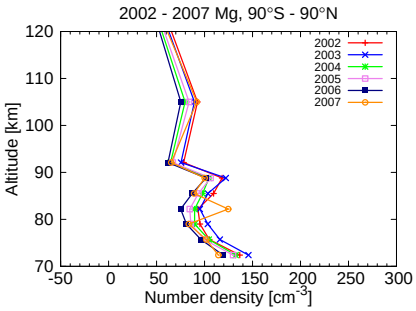

(b) Vertical profile of Mg from 70 to 120 km, linear altitude axis.

Figure 16: Vertical profiles of Mg^+ and Mg in the altitude range from 70 to 120 km. Note that the altitude axis is in linear scale now. Neutral Mg forms a layer around 89 km, as can be seen from the increased number densities at that altitude. The increased number densities of Mg observed in 2007 around 82 km cannot yet be explained. It should be noted, however, that the data sample of 2007 covers only January through April.

4.1.2 Seasonal variations of the total content

In the northern hemisphere, the total content of the ionized species shows a distinct seasonal variation with pronounced maxima in summer, see Figure 17(a) (shown are monthly averaged values, zonally averaged). Values of the total column increase from 3 – 4 $\cdot 10^9$ cm^{-2} to approximately $12 \cdot 10^9$ cm^{-2} during summer. The seasonal variation is strongest in the tropics and the polar region. Both latitudinal bins exhibit variations of more than $10 \cdot 10^9$ cm^{-3} , whereas the mid latitudes show a summer-winter difference of only 5 – 6 $\cdot 10^9$ cm^{-3} .

A seasonal variability is not observed in the southern hemisphere, however. Though the tropical latitudes 0° – 20°S (Figures 17(b) and 18(b)) show a similar seasonal variability as the northern tropical and mid-latitude regions, the pattern is much less pronounced at higher southern latitudes. On average over all southern latitudes, the Mg^+ shows rather irregular behavior (Figure 18(a)).

A corresponding seasonal variability is not observed in the neutral species Mg. Beside a weak variation between 20°N and 60°N (Figures 17(c) and (17(d)) which cannot be considered significant with respect to the total errors, no variation can be identified in either latitude region.

The regions of geomagnetic latitude $\geq$ 60° and $\leq$ -60° do not exhibit a different behavior as the corresponding hemispheres, see Figures 19(a), 19(b). In the northern geomagnetic cap, the seasonal cycle of Mg^+ is well pronounced, whereas the southern polar cap does not show any seasonal cycle. The neutral species can be considered constant with respect to the measurement errors.

4.1.3 Latitudinal distribution

Panel 20 shows the total column densities of Mg^+ versus geographical latitude for the two solstices and the two equinoxes and all years of observation. For all seasons, both magnesium species exhibit three maxima in the total column, two maxima near the polar caps around ±60° geographic latitude and one maximum near the equator. While the two polar maxima are located at constant latitudes throughout the year, the third maximum near the equator follows the position of the sub-solar point. The latter maximum will be referred to as "tropical maximum" in the following.

For the neutral species (see Figure 21), the three maxima are of similar magnitude for all years of observation. Additionally, within an individual year, all three maxima are of similar magnitude. The typical value of a single maximum is 1.5 – 2.0 $\cdot 10^9$ cm^{-2} .

The ionized species Mg^+ shows more variability. Whereas in all years of northern spring equinox observations, the northern and southern maximum are of rather similar magnitude of approximately 10^{10} cm^{-2} , northern autumn equinox as well as summer and winter favor the northern maximum. The northern summer maximum is a factor of two larger than the southern maximum. In 2002, an increase by a factor of four is observed. The southern maximum is of similar magnitude as the tropical maximum ($\approx 1.2 \cdot 10^{10}$ cm^{-2}) for the July measurements. The same values as for July hold for northern autumn equinox conditions in September. Around northern winter solstice in December, the northern maximum is a factor of approximately 1.5 larger than the other two maxima.

Figures 22 – 25 show zonally averaged number densities of both species for

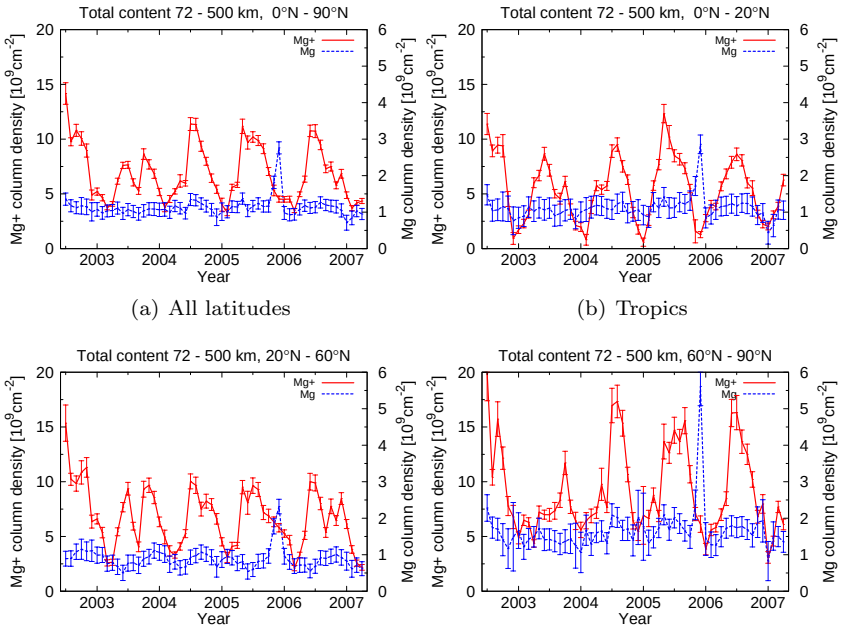

(a) All latitudes (b) Tropics

(c) Mid latitudes (d) Polar regions

Figure 17: Time series of the total column density of both magnesium species in the northern hemisphere. Each data point represents averages of one month of SCIAMACHY data. Annotated tickmarks denote January 1 of the corresponding year. Beside a total content series for the whole northern hemisphere, three individual latitude bands are considered: Tropics (0° – 20° N), mid-latitudes (20° – 60° N) and polar regions (60° – 90° N). As can be seen, Mg^+ exhibits a pronounced seasonal variation with summer maxima. The neutral species Mg does not show a significant seasonal cycle.

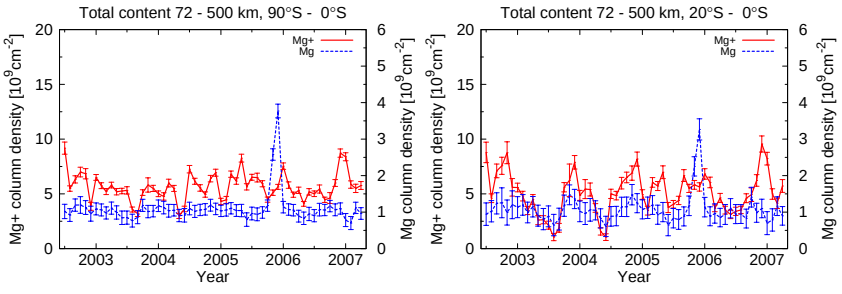

(a) All latitudes (b) Tropics

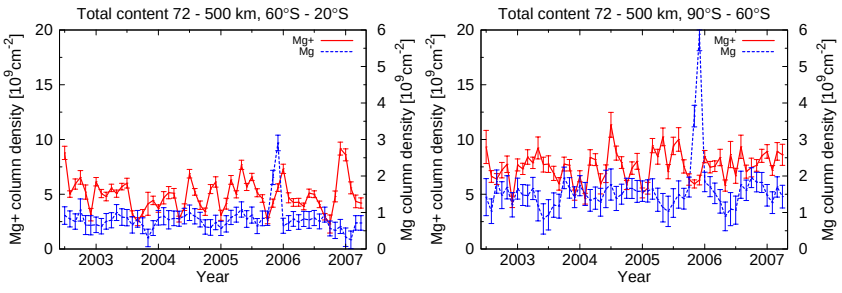

(c) Mid latitudes (d) Polar regions

Figure 18: Time series of the total column density of both magnesium species in the northern hemisphere. Tickmark setting, averaging and binning as in Figure 17. The seasonal variability of Mg^+ is much less pronounced in the southern hemisphere. The neutral species Mg does not show a significant seasonal cycle.

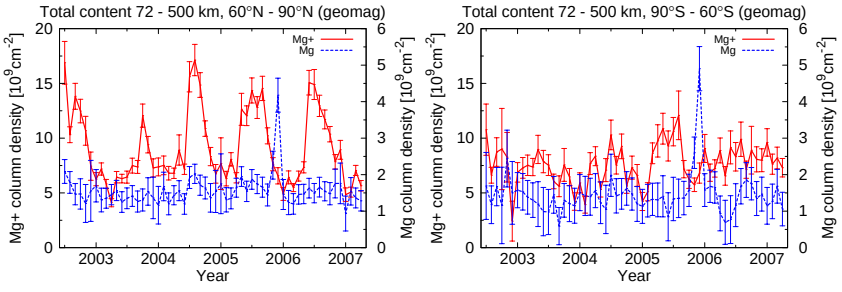

(a) Total contents of Mg and Mg^+ near the northern geomagnetic pole

(b) Total contents of Mg and Mg^+ near the southern geomagnetic pole

Figure 19: Time series of the total column density of both magnesium species for regions of geomagnetic latitudes $> 60°$. Tickmark setting and averaging in Figure 17. The northern hemisphere seasonal cycle is observed in the northern auroral oval as well, whereas the southern auroral oval does not show a seasonal cycle.

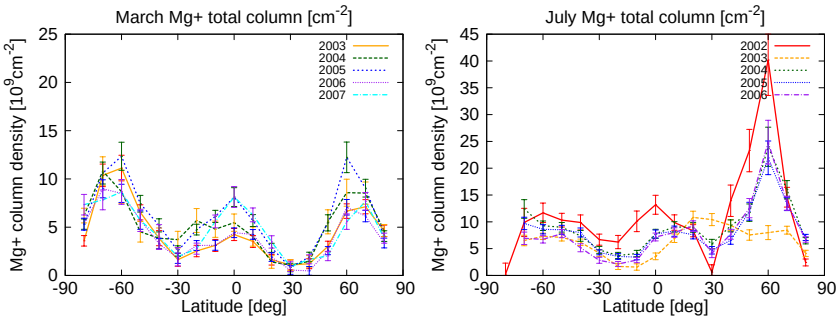

(a) March

(b) July

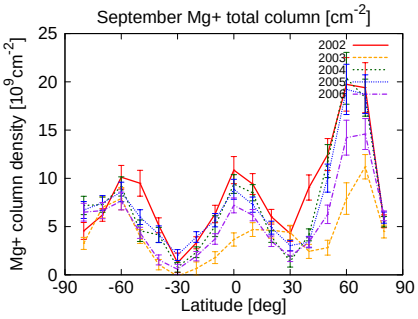

(c) September

Figure 20: Total column densities of Mg^+ versus latitude for March, July, and September. Three maxima near the equator and $\pm 60°$ are observed in each of the three plots. The Southern Atlantic Anomaly (see Section 3.7) is excluded.

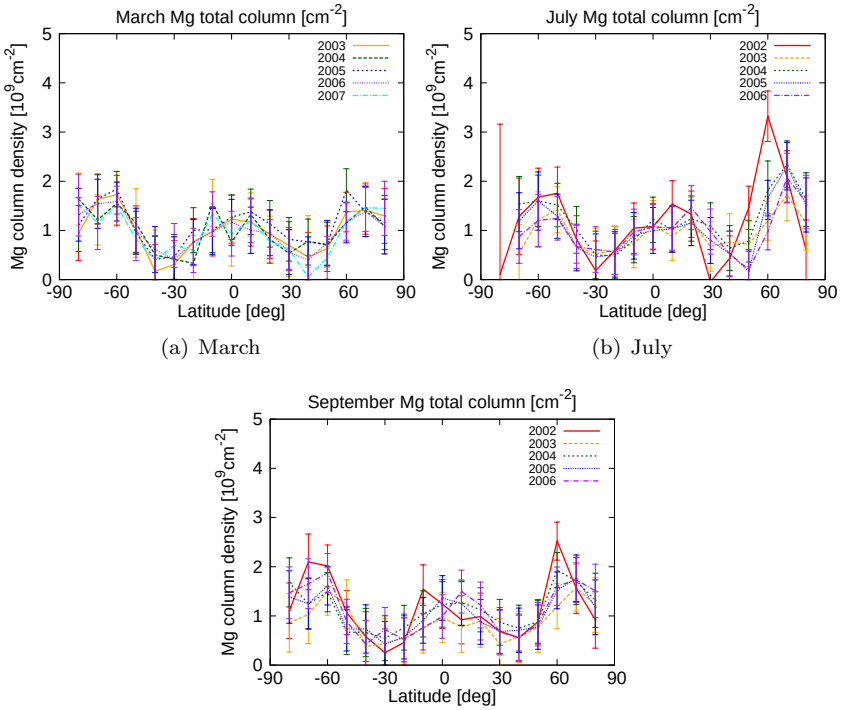

(a) March

(b) July

(c) September

Figure 21: Total column densities of Mg^+ versus latitude for March, July, and September. Three maxima near the equator and $\pm 60°$ are observed in each of the three plots. The Southern Atlantic Anomaly (see Section 3.7) is excluded.

equinox and solstice conditions. The data are averaged over a month (March, July, September and December, respectively) and binned to a 10° latitude grid. Note that the retrieval grid extends to 500 km altitude and the top pixel covers the range from 250 to 500 km (see Section 3.3). In this figure, the center altitudes of the individual pixels are given. Thus, the topmost number density is assigned to altitude (250+500)/2=375 km.

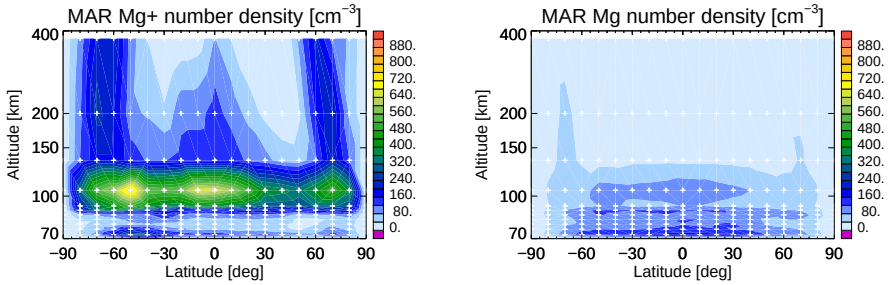

(a) Mg^+ latitudinal cross sections. (b) Mg latitudinal cross sections.

Figure 22: Zonally averaged number densities of Mg^+ (left panel) and Mg (right panel) during northern spring equinox. Values are averaged over March 2003 – 2007 and binned to a 10° wide latitude grid and an altitude grid that is derived from an averaged SCIAMACHY tangent altitude grid below 92 km. Above 92 km, a fixed altitude grid is used for the retrieval and the cross sectional plot. White crosses denote the center locations of the grid pixels. Note that the ordinate axis is in logarithmic scale. The Southern Atlantic Anomaly (see Section 3.7) is excluded.

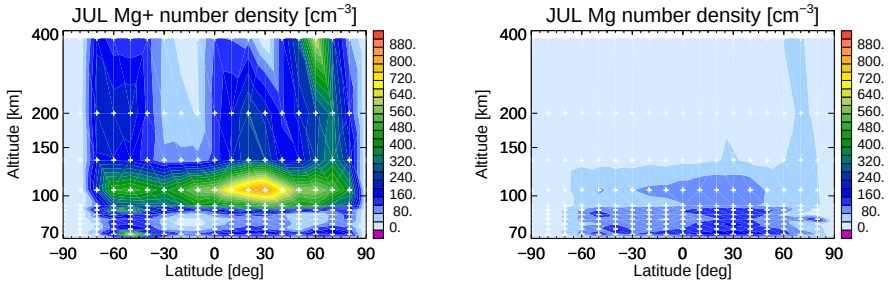

(a) Mg^+ latitudinal cross sections. (b) Mg latitudinal cross sections.

Figure 23: Zonally averaged number densities of Mg^+ during northern summer solstice. Values are averaged over July 2002 – 2006. Binning as in Figure 22(a).

The probably most striking feature in the Mg^+ distribution is a pronounced layer of Mg^+ centered around 100 km. Number densities within this layer are of the order of 400 – 700 cm^{-3} . It should be noted that the retrieval resolution is not sufficient to actually resolve the thickness of the layer.

This depiction allows to separate the contributions of different altitudes to the total column. The northern and southern maxima of column density can be identified (Figures 22(a), 23(a), 24(a), 25(a)). As can be seen, the increased number densities of Mg^+ are a result of a pronounced flow of Mg^+ out of the

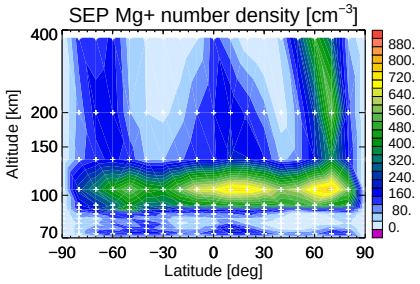

(a) Mg^+ latitudinal cross sections.

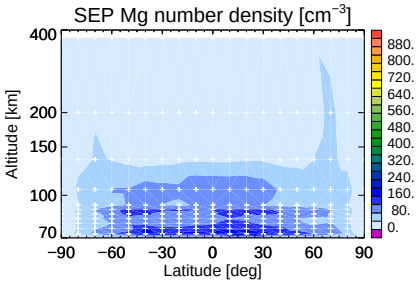

(b) Mg latitudinal cross sections.

Figure 24: Zonally averaged number densities of Mg^+ during northern autumn equinox. Values are averaged over September 2002 – 2006. Binning as in Figure 22(a).

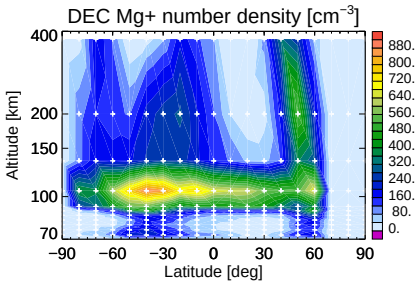

(a) Mg^+ latitudinal cross sections.

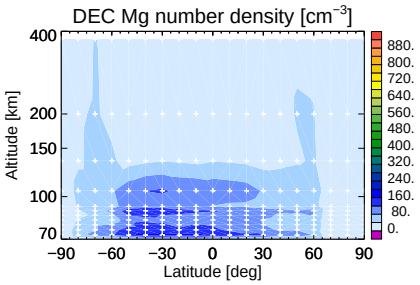

(b) Mg latitudinal cross sections.

Figure 25: Zonally averaged number densities of Mg^+ during northern winter solstice. Values are averaged over December 2002 – 2006. Binning as in Figure 22(a).

layer around 100 km to higher altitudes of up to 500 km. In the northern hemisphere, values of up to 500 cm^{-3} are observed at altitudes of up to 500 km. In the southern hemisphere, maximum number densities between 250 and 500 km are approximately 250 cm^{-3} . The same applies for the enhanced values of Mg^+ beneath the sub-solar point. The seasonally varying location of maximal values near the equator can be identified. Maximum values are 750 cm^{-3} , which is significantly larger than the average number density between 92 and 120 km.

The northern Mg^+ bloom is most intense during the second half of the year from July to December (Figures 23(a), 25(a), other months not shown). During January to June (Figure 22(a), other months are not shown here), the abundance of Mg^+ around 60° N is on average lower at all altitudes compared to the July to December values. Whereas the absolute number densities within the southern bloom, it can be observed that the extent in latitudinal direction is larger during January to June.

The distribution of neutral Mg exhibits largest number densities around the sub-solar point at low altitudes (Figures 22(b), 23(b), 24(b), 25(b)). The number density of Mg reaches values of 150 – 200 cm^{-3} near the sub-solar point. The abundance of Mg is below 40 cm^{-3} for tropical and mid-latitude regions above approximately 130 km.

The behavior of the Mg outflow at polar latitudes is different from that of the ionized species. For neutral Mg, the outflow over polar regions is only observed during summer. The January distribution (not shown here) shows an outflow above the southern polar cap, but not above the northern cap. The distribution of December is not as pronounced as in January. At least, Figure 25(b) exhibits an outflow to higher altitudes and over a wider latitude range above the summer pole. A contrary distribution occurs during July (Figure 23(b)). For equinox conditions in March and September (Figure 22(b) and 24(b)), the outflow is observable over both polar regions. It is much less pronounced and does not extend to the highest retrieval altitudes, however.

4.2 Discussion

The variations in the total column in the northern hemisphere can be attributed to an enhanced release of Mg from the reservoir species $Mg(OH)_2$. Higher summertime abundances of atomic hydrogen and reaction of this species with $Mg(OH)_2$ and MgOH release neutral Mg, see reactions (14) and (15). This enhanced density of Mg is not observed, however, as it is balanced by an increased rate of charge transfer with O_2^+ and NO^+ and a higher rate of photo-ionization (reactions (1), (2) and (3)).

In the southern hemisphere, the seasonal variations are damped by a mechanism that cannot be explained fully yet. In fact, a suitable mechanism is needed to retard just the summer enhancements. As can be seen from Figures 17(a) and 18(a), the winter total column is of similar magnitude of 3 – 4 $\cdot 10^9$ cm^{-2} in both hemispheres. The northern summer values, however, are increased by a factor of up to three (Figure 17(a)), in contrast to the southern total column densities (Figure 18(a)).

Removal of ionized Mg^+ by recombination is rather unlikely, as the number densities of electrons in the northern and southern hemisphere do not differ very much. The same applies for the abundance of the reaction partners for

charge transfer O_2^+ and NO^+. Thus, it cannot be assumed that different rates of charges transfer or recombination account for the absence of southern summer Mg^+ enhancement. A possible reaction to remove both Mg and Mg^+ is reaction with ozone (see reactions (5) and (10)).

The most peculiar feature of the Mg^+ distribution is the layer of large Mg^+ abundance around 100 km, within retrieval pixel 92 - 120 km (Figures 22 – 25). Note that the altitude resolution of the retrieval at this altitude is similar to the width of the pixel (see Section 3.6), thus the actual width and peak of the layer is not resolved. Model studies suggest the peak density to be located at approximately 95 km, with a full-width at half-maximum of approximately 4 km [Plane and Helmer, 1995], [Fritzenwallner and Kopp, 1998].

Figure 26 shows vertical profiles of major ionic species in the mesosphere and lower thermosphere. As can be seen, the number densities of ions is rather low below 85 km. The dominant amount of ionized species can be found above this altitude. The layer of Mg^+ around 100 km coincides with a rapid increase in the concentration of O_2^+ and NO^+ ions (Figure 26), which are the most important partners for charge transfer with neutral Mg. Below 90 km, the lifetime of Mg^+ is short because of reaction with ozone (reaction (10), see Section 2) and molecular oxygen (rection (6)). It can thus be concluded that above 90 km, the major amount of neutral Mg is ionized to form Mg^+. The ionic species is then deposited in an stable layer between 92 and 120 km.

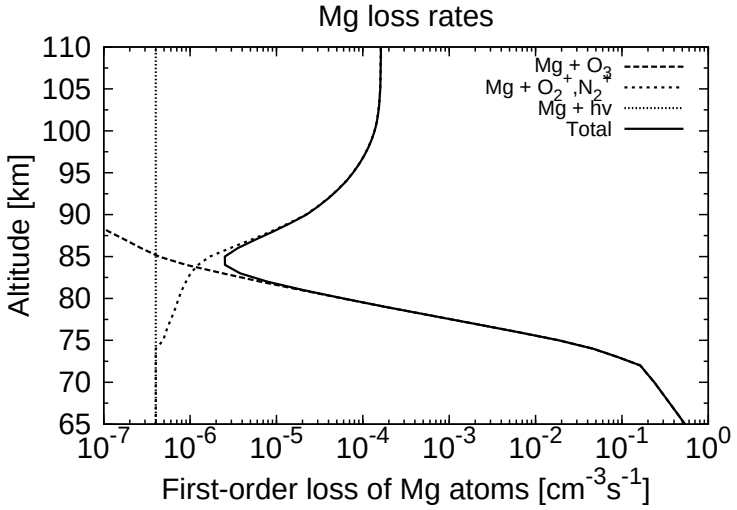

Figure 26: First-order loss rates of neutral magnesium in the mesosphere. Shown are loss rates for photoionization (fine-dotted, constant over the altitude range considered here), charge transfer with O_2 and NO^+ (dotted) and reaction with ozone (dashed). The solid line corresponds to the total loss rate. Note that there is a minimum in the total loss rate around 85 km. This results in an enrichment of neutral Mg around this altitude. Data for this Figure taken from Plane and Helmer [1995].

The Mg vertical profile exhibits a maximum around 89 km (Figures 15(b), 16(b)). This is suggested by model simulations and coincides with a minimum in the removal rate of neutral magnesium (see Plane and Helmer [1995] and

Section 8 for a discussion of removal rates for neutral magnesium). Assuming a constant source presented by influx of comic dust and a constant rate of descent by gravitational sedimentation, the enrichment of Mg at the altitude of minimum removal is self-evident.

A constant influx can be assumed safely since the occurrence of meteoric showers does not seem to have an impact on either magnesium species (see Section 7). It can thus be assumed that the major source of cosmic dust is asteroidal material from within the solar system. This assumption is supported by the work of McNeil et al. [1998] who propose the dominant influx velocity to be approximately 11 km/s, which is just the escape velocity of the Earth's potential well. They concluded that the major source of cosmic dust is a stationary source within the solar system. However, no publication was found that supported any large-scale inhomogeneities in the asteroidal material distribution within the solar system.

Both species show an enhancement in the number density towards lower altitudes (see Figures 15 and 16). In particular, the number densities at the lowest retrieval altitude of 70 km exceed the number densities in Mg at 89 km. This behavior can not be explained yet. Model studies [Fritzenwallner and Kopp, 1998], [Plane and Helmer, 1995] suggest an increasing number density of the reservoir species $Mg(OH)_2$ at lower altitudes (see reaction (11), Section 2). This is reasonable as potential partners for loss reactions of Mg^+ and Mg such as O_2, O_3 and H_2O are more abundant at lower altitudes. There is no hint that during the time of SCIAMACHY measurements an increased release rate from the reservoir species could have occurred. Note that the release rate is increasing with temperature and abundance of atomic hydrogen (see reactions (14) and (15)).

The enhancement may be a result of the ozone profile used in the retrieval scheme. To first order, the number density of the retrieval species is proportional to the product of the emitted radiance measured by the instrument and the extinction, i.e. $[N] \sim I \cdot e^{-\tau}$. Obviously, an under-estimation of the absorption would result in an over-estimation of the retrieval species. A drawback of the retrieval scheme presented in Section 3 is that a fixed ozone profile is used for all measurements. As ozone is considered to be the major absorption species at lower retrieval altitudes, increasing values in both Mg species hint to a systematic under-estimation of the absorption. Use of an comprehensive ozone climatology or even an ozone model – simultaneously driven to the retrieval – would help to shed light on this issue.

The outflow of Mg^+ ions near the equator has been discussed in Hanson and Sterling [1995]. However, Hanson and Sterling [1995] suggested the outflow to be restricted within a narrow region of $\pm 3°$ around the magnetic equator. The mechanism to lift the ions is based on the equatorial electrojet. The equatorial electrojet is an intense electric current which flows at approximately 100 km altitude over the magnetic equator. It consists of a daytime flow of electrons in the westward direction. It is driven by an eastward electric field which leads to the production of a vertical polarization field required in order to prevent the vertical flow of current. This polarization field is mathematically equivalent to the enhancement of the direct conductivity of the ionosphere between 95 and 120 km and is believed to be directly responsible for the intense eastward current.

It should be noted that Hanson and Sterling [1995] neglected neutral winds

within the source region of the ions around 100 km. However, this assumption is not feasible, as at 100 km, the ion-neutral collision frequency is still large enough that the ions bulk velocity is dominated by the neutral wind. Model runs carried out by Fesen et al. [1983] included a neutral wind across the equator and were able to show that the ions in fact can escape the source regions up to 30° away from the equator. This was confirmed by sporadic satellite observations [Fesen and Hays, 1982b], [Fesen and Hays, 1982a], [Gérard and Monfils, 1978]. It was proposed that the neutral wind pushes the ions up the magnetic field lines, thus allowing for further escape. The meridional circulation from the summer pole to the winter pole [Brasseur and Solomon, 1984] presents neutral winds in north-south direction. The occurrence of significant Mg^+ amounts above 150 km and outside a region of ±3–4° around the magnetic equator is thus consistent with the model results reported by Fesen et al. [1983].

The outflow of ionized magnesium over the regions of ±60° geomagnetic latitudes, i.e. the auroral ovals, cannot be explained fully yet. In 1985, in-situ measurements in polar regions were made using a retarding ion mass spectrometer (RIMS) on the Dynamics Explorer 1 (DE-1) spacecraft. As reported by Lockwood et al. [1985] and Moore et al. [1986], these measurements suggested a pronounced uplift of positive ions such as O^+ and H^+ over the auroral oval regions near the day side equatorward polar cap boundary. As this regions near the northern and southern geomagnetic pole present clefts in the magnetosphere and to let particles precipitate to lower altitudes, the effect was later named the "cleft fountain" [Lockwood et al., 1985].

Lockwood et al. [1985] and Moore et al. [1986] suggest that this fountain is basically driven by Joule heating near the auroral ovals. As a result of high conductivity within the auroral regions, strong current (the "auroral electrojets") systems are formed in the southern and the northern hemisphere, following the boundary of the auroral ovals defined by increased airglow intensities. The currents in the auroral ovals are part of large-scale ring currents in the magnetosphere. Friction of the electrons and the atomic and molecular species within these currents in the upper atmosphere leads to Joule heating in the auroral ovals in both hemispheres. The ions thus gain enough energy to escape the region of relatively high atmospheric density below 100 km, where the ionic motion is dominated by the neutral wind.

Once outside the neutral regime and within the cleft fountain, positive ions move along the magnetic field lines and the electric field lines and populate the polar magnetosphere. Though heavier species such as O^+ undergo convection and sediment down on the night side of the Earth, the fountain is suggested to present a loss mechanism for lightweight ions such as H^+ [Lockwood et al., 1985]. This presumption was supported by model calculations [Horwitz and Lockwood, 1985].

It should be noted that the in-situ observations of the RIMS instrument onboard the DE-1 satellite were carried out at high altitudes of 2000 km and more. The Mg^+ uplift observed by SCIAMACHY, however, is effective even at altitudes slightly above 100 km. Thus, the results found by Lockwood et al. [1985] and others cannot be transferred directly to explain the "Mg^+ polar fountain". The basic mechanisms that produce the cleft fountain such as Joule heating apply to the lower thermosphere at 100 km as well, however. In addition, the motion of ions above 100 km is not dominated by the neutral motion but by E and B fields. Thus, it is not unreasonable to suggest that the Mg^+ outflow

is closely associated with the O^+ fountain observed near the auroral regions.

Figure 27 gives a graphical review of the two major processes of Mg^+ uplift.

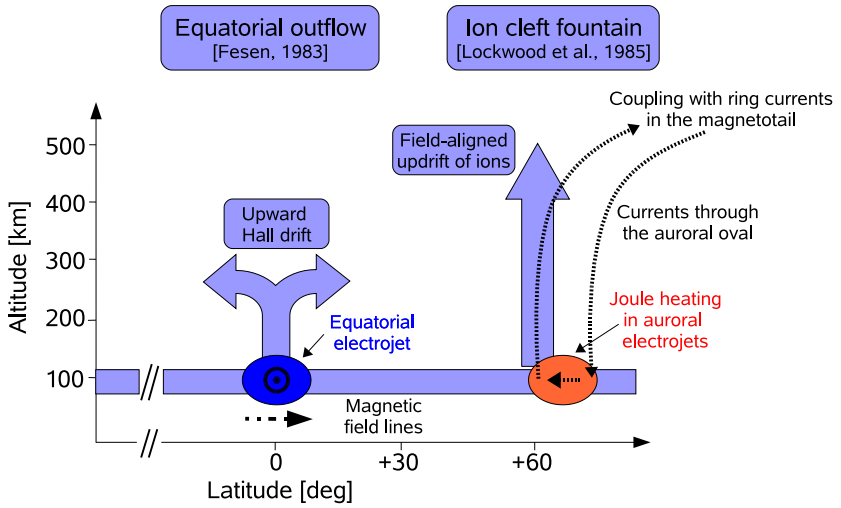

Figure 27: Simplified review of the major uplift processes for Mg^+. The equatorial fountain was suggested by Hanson and Sterling [1995]. The simplified approach of Hanson and Sterling [1995] was extended later to explain increased number densities of Mg^+ at high altitudes and higher latitudes by [Fesen et al., 1983]. The polar outflow was first discussed by Lockwood et al. [1985], this work features the term "cleft fountain" for the first time. See text for details of uplift mechanisms.

4.3 Mg / Mg^+ measurements in the lower thermosphere

A new state was defined for SCIAMACHY limb measurements which enables measurements of emission signals throughout the mesosphere and lower thermosphere. For this new state, the limb sequence of SCIAMACHY was shifted to scan the altitude range from 60 km up to 150 km in 30 steps, i.e., with the same vertical spacing as in the normal stratosphere-mesosphere mode. 20 orbits of this new state were carried out on August 8 and 9, 2007, to test the viability of this new scanning mode to measure up into the lower thermosphere. Mg and Mg^+ number densities from these 20 orbits were retrieved using the tomographic retrieval described in Section 3; preliminary results for the resulting average latitudinal cross-sections from 70 - 400 km are shown in Figure 28 for Mg^+, and in figure 29 for Mg.

Generally, the features observed during these 20 orbits compare well with the July average data for 2002-2006 as shown in Figure 23. However, as the vertical resolution is much better in the altitude range from 90 - 150 km, the main structures are resolved much better, and an additional feature is observed around 150 - 200 km. The main feature of the Mg^+ distribution is still the layer between 90 - 120 km; this is now resolved to be centered around 100 km, at slightly higher altitudes than expected from the model results [Plane and Helmer, 1995; Fritzenwallner and Kopp, 1998]. Another strong feature observed

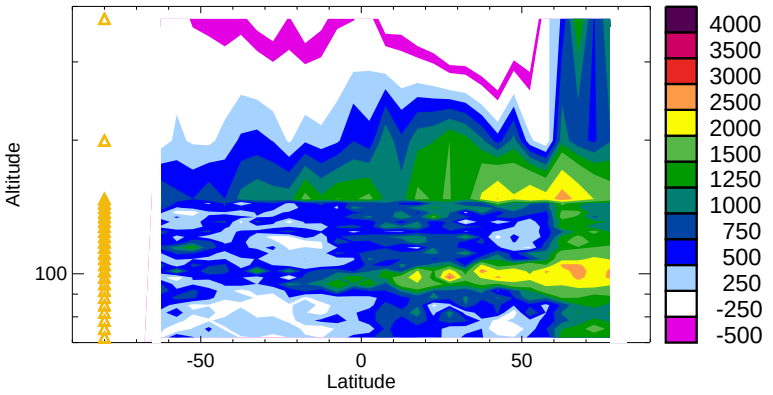

Figure 28: Mg^+ mean number densities (cm^{-3}) from 20 orbits with the new SCIAMACHY mesosphere-thermosphere state, measured on August 8 and 9, 2007, averaged over 5 degrees in latitude. Yellow triangles denote the center of the retrieval altitude grid boxes. Clearly observed are two layers of enhanced values of Mg^+, one around 100 km, the other between 150-200 km; also, two branches of updrift of Mg^+, one in northern polar regions reaching from 70 km up to at least 400 km, the other in northern tropics and subtropics, reaching from 70 km up to the layer above 150 km.

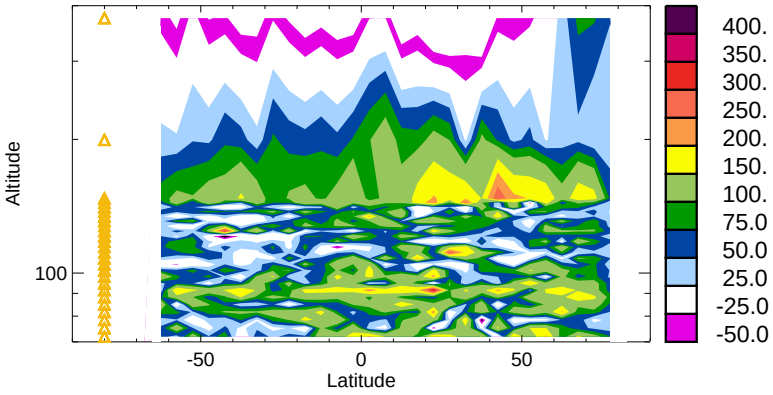

Figure 29: Mg mean number densities (cm^{-3}) from 20 orbits with the new SCIAMACHY mesosphere-thermosphere state, measured on August 8 and 9, 2007, averaged over 5 degrees in latitude. Yellow triangles denote the center of the retrieval altitude grid boxes. Clearly observed are two layers of enhanced values of Mg, one around 90-92 km, the other between 150-200 km; also, one branch of updrift of Mg, in northern polar regions reaching from around 200 km up to at least 400 km.

in the long-time mean as well as in the measurements with the new state is the updraft of Mg^+ in polar latitudes and around the magnetic equator. Additionally, another layer of enhanced Mg^+ is observed around 150-200 km altitude in the measurements of the new state that could not be resolved with the normal SCIAMACHY limb mode; this feature reaches from the Mg^+ updraft in northern polar latitudes down to southern midlatitudes, with highest number densities in northern high latitudes. A corresponding layer of high values of Mg is observed in the same altitude range with a similar latitudinal behavior. Apart from that, the Mg measurements from the new state show a rather patchy behaviour, the only clear features apart from the layer between 140-200 km being an upward pointing branch of high values at high altitudes in northern polar latitudes, between 200-400 km altitude; this feature is also showing up in Mg^+; and a thin layer of enhanced Mg values around 90-92 km reaching from northern to southern polar latitudes, with a maximum in northern subtropics. The layers of Mg and Mg^+ around 140-200 km as well as the apparent updrift of neutral Mg in northern high latitudes were rather unexpected. To determine whether these are common features of the Mg / Mg^+ distribution, it will be proposed to drive the new mesosphere-thermosphere state of SCIAMACHY on a regular basis in the future.

5 Correlation with solar activity

The solar radiation is subject to variations of intensity. This holds for all wavelength regions. However, shorter wavelengths are subject to larger variations. During a 11-year solar cycle, the 200 – 300 nm irradiance changes by 10%, the Lyman-α hydrogen emission line at 121 nm varies by up to 30%. As the shorter wavelengths render a large input of energy into the Earth's atmosphere, it is reasonable to investigate the impact of solar variations on the magnesium content in the upper atmosphere. Additionally, the impact of variations of the particle flux from the Sun, the so-called solar wind is discussed. The solar wind consists of both electrons and protons and affects the atmosphere at all levels.

A convenient proxy of the solar activity rendered to be the intensity of the solar electromagnetic radiation at 10.7 cm wavelength (i.e. $\approx$ 2800 MHz). It has been found that this emission correlates with the daily sunspot number and is determined by the same mechanisms and processes affecting the visible and X-ray wavelength range [Tapping and Murdin, 2000]. Additionally, the radio fluxes in the 1000 – 9400 MHz range correlate well with the total solar irradiance [Schmahl and Kundu, 1994].

This emission is routinely observed by ground-based stations since the late 1940's. Thus, an extended time series from a number of different sources is readily available. In this section, the time series generated by the Dominion Radio Astrophysical Observatory near Penticton, Canada is used. This observatory is operationally measuring the 10.7 cm flux since the late 1960's. See [Covington, 1969] for a review of the measurement technique and the data processing procedure. Figure 30(a) shows the radio flux intensity during the SCIAMACHY operation.

As a result of the rather low energy of the 10.7 cm radio flux (E(10.7cm) = $1.2 \cdot 10^{-15}$ eV, E(300nm) = 4.13 eV), the chemistry of the upper atmosphere is not directly affected by solar radiation of this wavelength. Within this section,

the 10.7 cm flux will be used rather as a proxy for higher energetic radiation inserting energy into the upper and middle atmosphere.

A direct and strong impact can be attributed to particle fluxes from the Sun. While the lower energetic solar plasma fluxes in the interplanetary space only vary slowly with the solar cycle, the flux of high-energetic solar particles increases significantly after erratically occurring Earth-directed solar flares and coronal mass ejections. The charged solar particles can enter the Earth's atmosphere through the polar cusps. The edge of the entering regions coincide to a good approximation with a geomagnetic latitude of $\pm$ 60° . Inside the polar cusps, the particles can penetrate into the atmosphere, cause ionizations and dissociations, and affect the atmospheric ion and neutral chemistry down to stratospheric levels. Therefore variations of the energetic solar particle fluxes influence the ionospheric conditions in the polar regions, and may have subsequent impacts on the Magnesium species in the MLT. See Figure 30(b) for a time line of the proton fluxes with different energies during the SCIAMACHY mission.

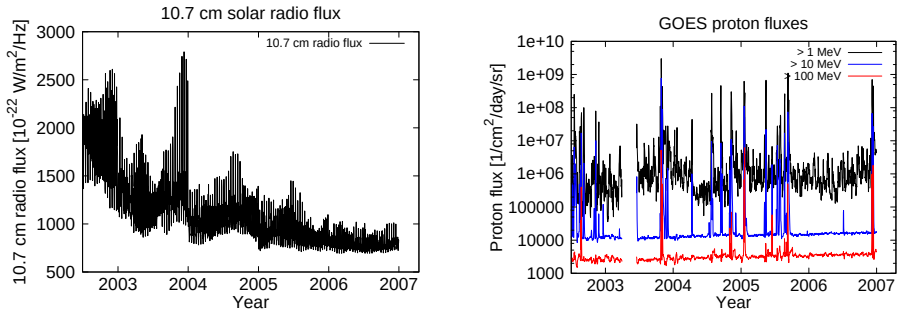

(a) 10.7 cm radio flux.

(b) GOES proton fluxes.

Figure 30: Left panel: Radio emission intensity at 10.7 cm (2800 MHz), as measured by the Dominion Radio Astrophysical Observatory, Penticton, Canada. Tick marks indicate Jan 1 of each year. On average, the intensity of the radio flux is decreasing, indicating an approach to the next solar minimum of the 11-year solar cycle. Increased values of the flux are observed at the end of 2003 during a turbulent period of the Sun. Data obtained from Dominion Radio Observatory, Penticton, Canada [2007]. Right panel: Solar proton flux intensity as measured by GOES 12 instrument. Shown are proton fluxes for proton with energies > 1, > 10 and > 100 MeV. Tick marks indicate Jan 1 of each year. Separated solar proton events are clearly visible. The largest peak near the end of 2003 marks the October 2003 solar proton event. See Section 6 for a discussion of the impact of this SPE on the magnesium abundance in the mesosphere and lower thermosphere. Data obtained from NOAA/National Weather Service [2007].

Within the next section, the linear correlation between the magnesium species content and the solar activity will be investigated using the Pearson correlation index r. See Scharringhausen [2007] for a detailed mathematical formulation. A value of r near unity indicates a strong correlation between the two quantities under consideration whereas $r = -1$ indicates an anti-correlation. It should be noted that the correlation coefficient r does only quantify the linear correlation.

Any other functional relation between the two quantities under consideration may exist, but cannot indicated by the Pearson correlation coefficient.

5.1 Correlation with proton fluxes

5.1.1 Globally averaged total column content and proton fluxes

Figures 31 and 32 show scatter plots of the Mg^+ respectively Mg global total column content versus the proton flux intensity in different energy ranges. The plots show all daily averaged measurements available from July 2002 until April 2007. As can be seen from the plots as well as from the corresponding correlation coefficients (given in the captions, values are in the range 0.05 – 0.12), no linear correlation can be found. Though there are a number of events of high proton flux especially within 100 MeV band (see Figures 31(b), and 32(b)), no corresponding events of high Mg^+ or Mg content are associated with these episodes.

The corresponding scatter plots do not suggest any other functional relation between the magnesium content and the proton fluxes.

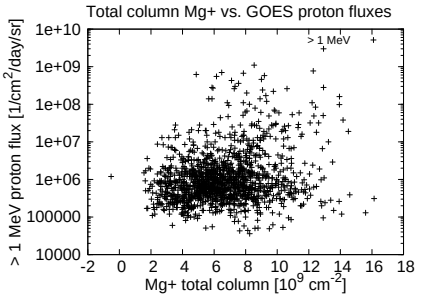

(a) Mg^+ content and proton flux for energies > 1 MeV. The correlation coefficient is $r \approx 0.12$, indicating no linear correlation.

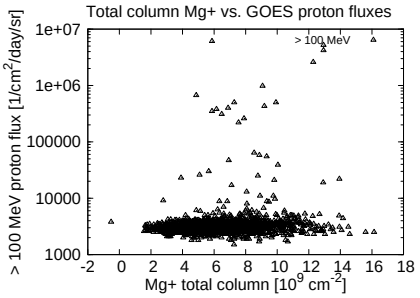

(b) Mg^+ content and proton flux for energies > 100 MeV. The correlation coefficient is $r \approx 0.08$, indicating no linear correlation.

Figure 31: Scatter plots of the Mg^+ total column content versus the solar proton fluxes in different energy bins. As can be seen from the plots as well as from the correlation coefficients, there is no linear correlation between the total Mg^+ column and the solar proton fluxes.

5.1.2 Vertical profiles and proton fluxes

Figures 33(a) and 33(b) show the correlation indices for Mg^+ and Mg at different altitudes with the 1 MeV, and the 100 MeV solar proton flux. All measurements are averaged daily and binned into five categories. These consist of four geographical latitude ranges and the geomagnetic polar regions, i.e. regions of geomagnetic latitude $> 60°$.

Consistently with the total columns, the vertical profiles do not exhibit any correlation between the Mg^+ or Mg number density at different altitudes and the solar proton fluxes. This is the case for all latitude ranges and all proton energies.

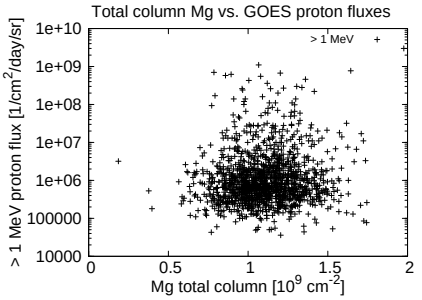

(a) Mg content and proton flux for energies > 1 MeV. The correlation coefficient is $r \approx 0.06$, indicating no linear correlation.

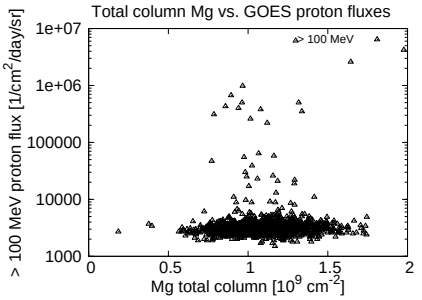

(b) Mg content and proton flux for energies > 100 MeV. The correlation coefficient is $r \approx 0.07$, indicating no linear correlation.

Figure 32: Scatter plots of the neutral Mg total column content versus the solar proton fluxes in different energy bins. As can be seen from the plots as well as from the correlation coefficients, there is no linear correlation between the total Mg column and the solar proton fluxes.

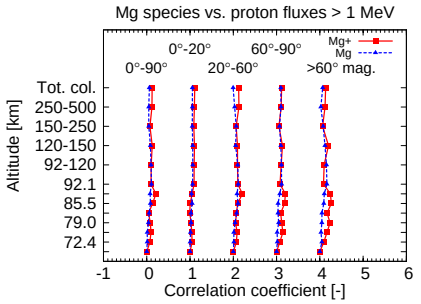

(a) Correlation indices for Mg^+ (solid, squares) and Mg (dashes, triangles) contents at different altitudes and the solar proton flux for protons with energies $>$ 1MeV.

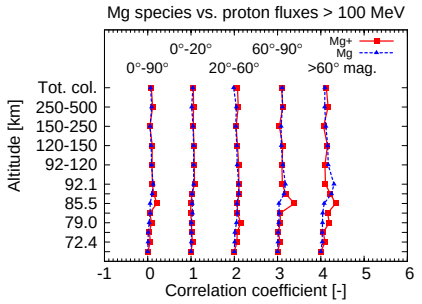

(b) Correlation indices for Mg^+ (solid, squares) and Mg (dashes, triangles) contents at different altitudes and the solar proton flux for protons with energies $>$ 100 MeV.

Figure 33: Correlation indices for Mg^+ (solid, squares) and Mg (dashes, triangles) contents at different altitudes and the solar proton fluxes for protons with energies > 1 MeV and 100 MeV, respectively. All correlation indices are well below 0.5, indicating no or a weak linear correlation between Mg species and the proton flux. Curves corresponding to different latitude bands are shifted to the right by multiples of unity for convenience.

5.2 Correlation with the 10.7 cm radio flux

5.2.1 Total column content and 10.7 cm radio flux

Figure 34 shows scatter plots of the Mg^+ respectively Mg total column content versus the radio flux at 10.7 cm. Used are all measurements of Mg^+ and Mg being available from the start of the mission. The measurements are daily averaged to reduce the amount of data. Approximately 1700 data points enter each plot. The linear correlation index between Mg^+ and the radio flux is 0.67, indicating a very weak linear correlation. For neutral Mg, $r = 0.51$ holds. Note that the vertical axis in Figures 34(a) and 34(b) is given in linear scale. This explains why Figure 31(a) and 32(a), exhibiting a similar structure, correspond to lower correlation indices each.

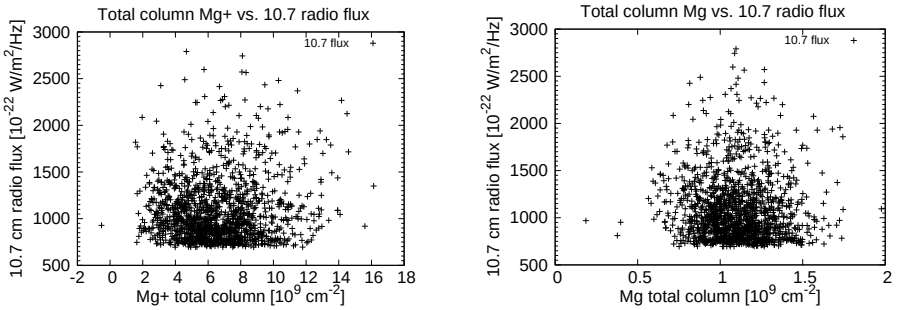

(a) Mg^+ content and 10.7 radio flux.

(b) Mg content and 10.7 radio flux.

Figure 34: Left panel: Mg^+ content and radio flux. The correlation coefficient is r$\simeq$ 0.67, indicating a weak linear correlation. Right panel: Mg content and radio flux. The correlation coefficient is r$\simeq$ 0.51, indicating a very weak linear correlation. Note that in both panels the abscissa axis is given in linear scale.

5.3 Vertical profiles and 10.7 cm radio flux

Figure 35 shows the correlation indices for Mg^+ and Mg at different altitudes and the 10.7 cm radio flux. All data are averaged and binned as for Figures 33(a) and 33(b).

Both species show maximal correlations with the solar radio flux at altitudes between 92 and 120 km. Mg^+ exhibits a secondary maximum around 75 km. Maximal correlation indices of Mg^+ and Mg between 92 and 120 km are found to be approximately 0.7, indicating a moderate linear correlation. Above 120 km, correlation indices of Mg^+ and Mg decrease to values of 0.3 – 0.4 again. Note that the correlation profiles are relatively independent from the latitude band. The general shape and the magnitudes are identical for all five categories.

These results are consistent with those of Minschwaner et al. [2004]. Measurements carried out in 1999 by the ISAAC (Ionospheric Spectroscopy And Atmospheric Chemistry) instrument onboard the ARGOS satellite as presented by Minschwaner et al. [2004] suggest similar correlation indices. The ISAAC measurements provided a correlation index of $r = 0.62$ between the Mg^+ total thermospheric column along the limb line-of-sight at 102 km tangent altitude and the solar soft X-ray flux between 2 and 7 nm. The correlation between the

Lyman-α flux and the Mg^+ slant column density was found to be maximal at 120 km with $r = 0.71$.

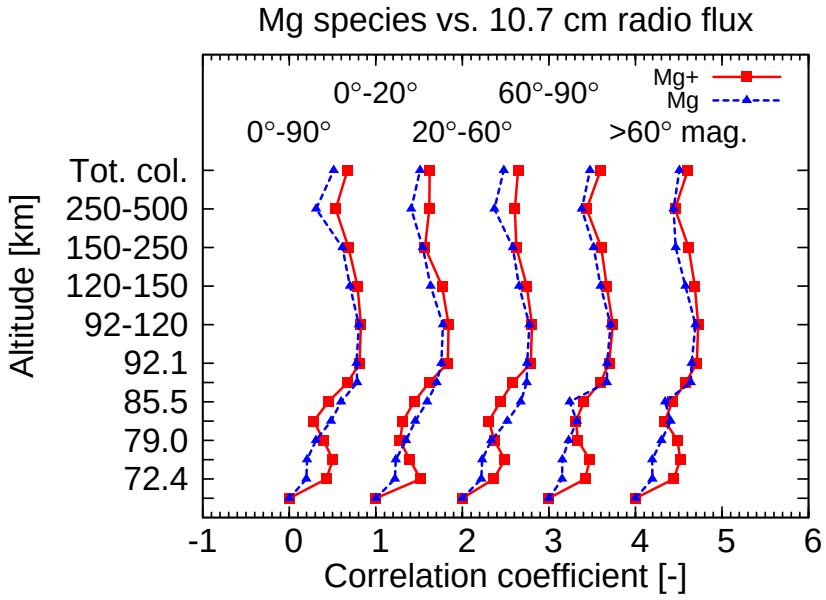

Figure 35: Correlation indices for Mg^+ (solid, squares) and Mg (dashes, triangles) contents at different altitudes and the solar radio flux at 10.7 cm. Curves are shifted as in Figure 33(a). The correlation indices for both species are maximal between 92 and 120 km. A secondary maximum is present for Mg^+ around 75 km.

5.4 Conclusions

No significant correlation between the solar activity and the Mg^+/Mg abundance in the upper atmosphere has been found. It should be noted, however, that only a small part of the 11-year solar cycle is covered by the SCIAMACHY measurements. The mission started in 2002, at the maximum of solar cycle no. 23. The latest measurement available for this work was done in April 2007. Thus, not even a complete cycle is covered. What can be concluded from the investigations carried out in Sections 5.1 and 5.2 is that variations on small time scales of five to six years do not affect the magnesium total content.

The absence of a strong correlation between the solar proton flux and the Mg^+ content does not contradict the findings presented in Section 6. There, observations made during a Solar Proton Event exhibiting a significant increase of both magnesium species are presented. As a result of the extreme nature of Solar Proton Events with respect to particle fluxes and impacts on the thermosphere, mesosphere and stratosphere in general, periods of strong proton fluxes such as in October/November 2003 may still affect the magnesium content and distribution in the upper atmosphere.

6 Solar proton events and upper atmosphere magnesium

This section describes the impact of a strong solar outburst in October 2003 on the chemistry and physics of mesospheric and thermospheric magnesium.

As it has been mentioned in Section 5, the energetic charged solar particles are able to enter the Earth's atmosphere via the polar cusps. The main constituents of the high-energetic solar plasma fluxes are energetic protons, though energetic electrons and heavier nuclei such as ionized helium species may accompany the protons. However, it is assumed that the atmospheric impact of these solar phenomena is mainly a result of the flux of energetic protons. The particles exhibit energies reaching from tens of keV to several MeV. Thus, these particle bursts are often called *Solar Proton Event (SPE)*. The high-energetic fraction of these particles has enough energy to penetrate the atmosphere down to the upper and middle atmosphere, i.e. the stratosphere and mesosphere. Chemical interactions result in increased production of both HO_x (H,OH, HO_2) and NO_y (NO, NO_2, NO_3 and others) species. These species eventually lead to ozone depletion (see e.g. Jackman et al. [2005]).

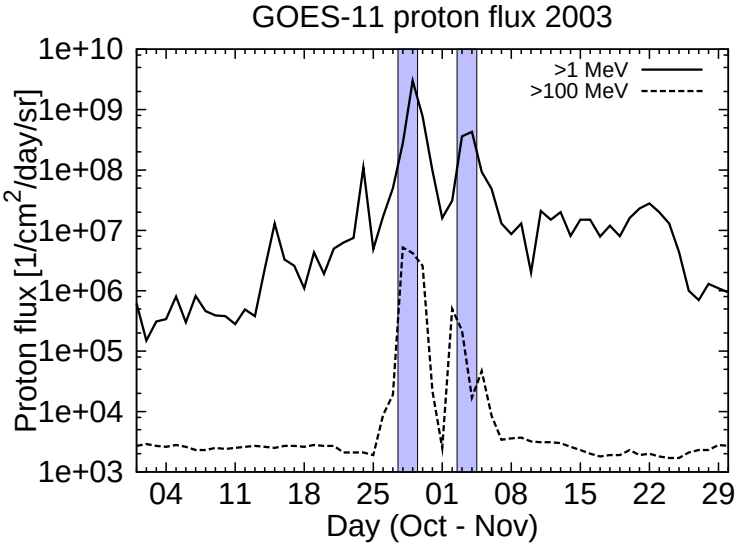

Figure 36: The GOES 11 proton flux measurements for October and November 2003. The solid line corresponds to proton energies > 1 MeV. The flux of these particles increases by a factor of $100 - 1000$ within few days. The increase in high energetic protons (energies > 100 MeV) is four to five orders of magnitude. Both proton fluxes exhibit two distinct maxima on October 29 and November 3/4. The high-energetic protons exhibit a maximum on November 3, whereas the low-energetic particle flux is maximal on November 4. These energy bins have been chosen such that the particles deposit the bulk of their energy in the mesosphere and lower thermosphere (1 MeV) respectively the upper stratosphere (100 MeV).

Shortly after the last maximum of the solar cycle in 2002, the Earth encountered a strong SPE in October 2003. It started on October 28 and lasted until

October 30. The maximum occurred on October 29. Another event – about an order of magnitude smaller with respect to the particle fluxes – occurred shortly after, with a maximum on November 3rd. Both maxima are clearly visible in Figure 36, depicting the proton flux as measured in 2003 by the GOES-11 satellite instrument. The October 29 increase in proton flux is clearly visible. Fluxes in both proton energy regimes shown here increase by two to three orders of magnitude. It should be noted that the bulk of the low-energetic protons of 1 MeV deposit their energy at altitudes between 85 and 90 km, whereas the energy loss of the high-energetic protons is confined to altitudes below 60 km.

6.1 Observations

This section presents observations made using the SCIAMACHY instrument during October and November 2003. Globally averaged Mg and Mg^+ abundances and the distribution of magnesium species within regions of high geomagnetic latitude (i.e. $\geq 60^\circ$) are presented. See Scharringhausen [2007] for a more detailed view on the behaviour of both magnesium species in tropical regions, mid latitudes and polar regions.

6.1.1 Global view - all latitudes, $0^\circ \leq |\varphi| \leq 90^\circ$

On a global scale, the effect of the October 29 SPE is clearly visible in the total content of both Mg^+ and Mg, see Figure 37. Both Mg^+ as well as Mg show high abundances during the time of the October 29 event. The increase is especially pronounced in the neutral magnesium column. The total column content is increased by a factor of four compared to the average column content during October and November. The variation in Mg^+ during 'quiet' times (i.e. times without strong proton fluxes) is larger, however. Values of Mg^+ column content vary between $2 \cdot 10^9$ and 10^{10} cm^{-2} between October 1 and October 26 respectively November 6 and November 30. The maximum column density of approximately $1.3 \cdot 10^{10}$ cm^{-2} is observed during the October 29 event, though.

The November 3/4 event is not visible in the total content data, however. Both Mg and Mg^+ values decrease between November 3 and 4. Both species show increased values at November 5. However, in case of neutral magnesium, the error is rather large compared to the absolute value, thus the increase is not considered significant. The increase in Mg^+ is significant, but does not exceed the usual variation during the two months considered.

Higher abundances of both Mg species occur in particular at low altitudes, i.e. below 100 km, see Figures 38, 39, and 40, 41. Within the altitude range from 70 to 85 km, neutral Mg increases to values of 200 cm^{-3} on October 29. This a factor of 5 more compared to the average values in October and November ($\approx$ 40 cm^{-3}). Singly ionized magnesium is more abundant below 85 km as well. Absolute values do not exceed 250 cm^{-3}, though. A strong increase in Mg^+ occurs at altitude 89 km, where a pronounced peak is observed during October 29. This peak is neither present one day before nor one day after. Significantly increased values at very high altitudes of approximately 400 km are observed on October 29 as well as October 28 and October 30. The Mg^+ number densities at 400 km reach approximately 400 cm^{-3} on October 28 – 30. This is a factor of three to four more than the average values of October ($\approx$ 80 cm^{-3}) and November ($\approx$ 110 cm^{-3}).

Though the total content is not significantly increased during the November 3/4 event, increased Mg values at altitudes between 70 and 85 km are observed, see Figure 42. The absolute values are lower than on October 29, though. Concentrations of Mg^+ are increased significantly at altitudes around 100 km. However, no increase at 89 km is observed. High altitude values of neither Mg nor Mg^+ are increased significantly.

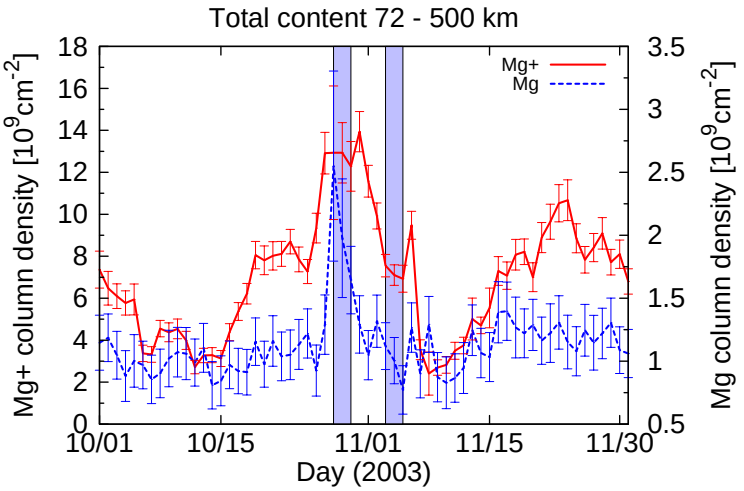

Figure 37: Total column amount of Mg^+ (solid) and Mg (dashed) seen during October and November 2003 **averaged from 90°S – 90°N geographical latitude and all longitudes.** Blue strips refer to the first and second SPE under consideration, i.e. the time periods October 28 – 30 respectively November 3 – 5. Maximum proton fluxes occurred on October 29 and November 4, see Figure 36. Significantly increased total column contents of both Mg species are observed on October 29, these constitute the maximum values during October and November 2003. On November 6, however, increased column amounts of Mg^+ are observed.

6.1.2 Geomagnetic latitudes $60° < |\varphi_{\mathbf{magnetic}}| \leq 90°$

The total content of both species is maximal on October 28 (Figure 43). The Mg^+ content at that day ($3.2 \cdot 10^{10}$ cm^{-2}) is a factor of three above the October/November average (10^{10} cm^{-2}). The same holds for the neutral Mg total content, this is increasing from a background level of $2 \cdot 10^9$ cm^{-2} to values of $6 \cdot 10^9$ cm^{-2}.

The November 3/4 SPE does not impact the total content of either species significantly (Figure 43). Weak effects are observed at low altitudes between 70 and 120 km, see Figure 48. The deviations to the October and November averages, however, are smaller than those during the October 29 event.

Mg^+ values are increased at all altitudes (Figures 44, 45). The 89 km layer of October 29 is broader compared to the other geographical regions (Figures 46 and 47). Maximal Mg^+ abundances do not occur at 120 km solely anymore. However, an equal abundance is observed at higher altitudes of 150 km.

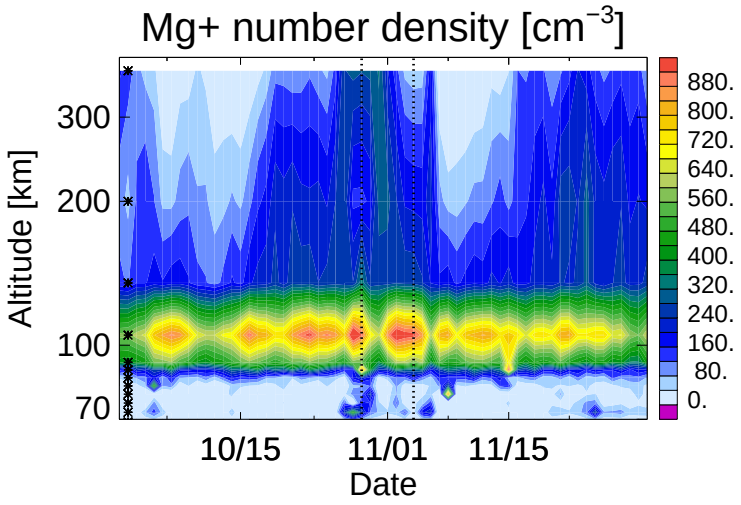

Figure 38: Average vertical distribution of Mg^+ during October and November 2003 **averaged from 90°S – 90°N geographical latitude and all longitudes.** Asterisks on the left denote the center altitudes of the retrieval pixel grid, see Section 3.3. Increased values occur primarily at low altitudes below 120 km. A short-lived layer of Mg^+ is observed at approximately 89 km altitude on October 29.

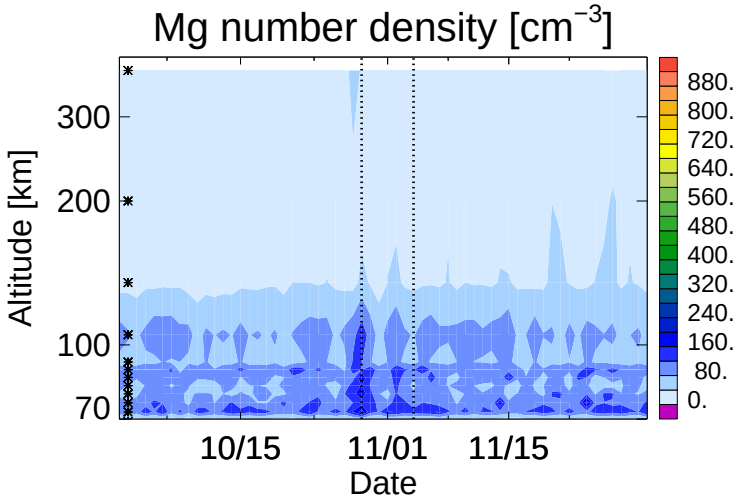

Figure 39: Average vertical distribution of Mg during October and November 2003 **averaged from 90°S – 90°N geographical latitude and all longitudes.** Asterisks on the left denote the center altitudes of the retrieval pixel grid, see Section 3.3. Increased values of neutral Mg are observed at all altitudes up to 120 km during the first event.

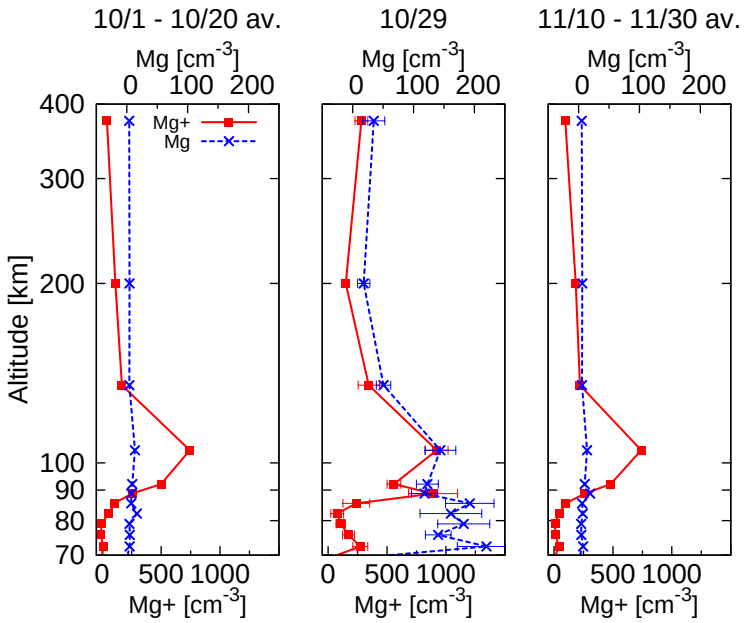

Figure 40: Average vertical profiles of Mg^+ (solid) and Mg (dashed) during October 10 – 20, October 29 and November 10 – 20, **averaged from 90°S – 90°N geographical latitude and all longitudes.** A pronounced layer of Mg^+ occurs on October 29 at an altitude of 89 km. Vertical profiles of both Mg^+ and Mg are increased during the solar proton event below 100 km.

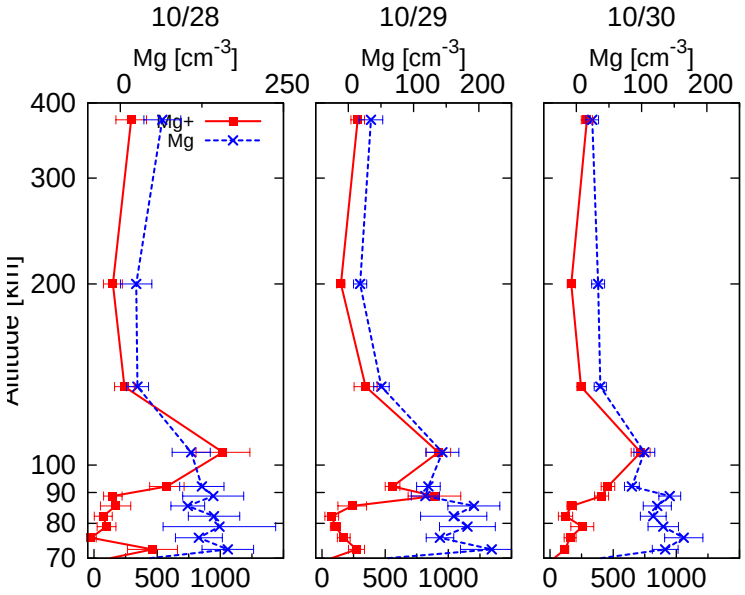

Figure 41: Daily average vertical profiles of Mg^+ (solid) and Mg (dashed) during October 28 – 30, **averaged from 90°S – 90°N geographical latitude and all longitudes.** A pronounced short-lived layer of Mg^+ at 89 km altitude is observed on October 29. Maximum values of both species at 400 km altitude are observed on October 28.

It should be noted that the impact of the SPE on high altitude Mg species is highest on October 28, see Figures 44 and 45. Values of neutral Mg at 400 km have already dropped to October average values on October 29. The Mg^+ concentration at 400 km is still high at that time, though smaller than the October 28 abundance. On October 30, values of Mg^+ are back to average as well.

6.1.3 Summary of observations during October/November 2003

Both species show significantly increased values during the October/November 2003 period of intense solar activity and strong particle fluxes. Abundances of neutral Mg are increased by more than a factor of 10 on October 29 at altitudes below 150 km. Increased values are observed at very high altitudes around 400 km as well for all three days of the first SPE. The strongest increase in Mg^+ is observed between 89 and 120 km. Values are high for all three days of the first event. On October 29, a pronounced layer of Mg^+ is formed around 89 km. The full-width-half maximum of this layer is smaller than or equal to the vertical resolution of the retrieval, which is approximately 5 km. This can be seen from the fact that the values at the adjacent altitudes (92 and 86 km) do not differ significantly from the values on October 28 and October 30, where no peak at 89 km is observed.

The total content exhibits increases of both species on October 29. As could be expected, the largest variations compared to the average are observed in polar regions.

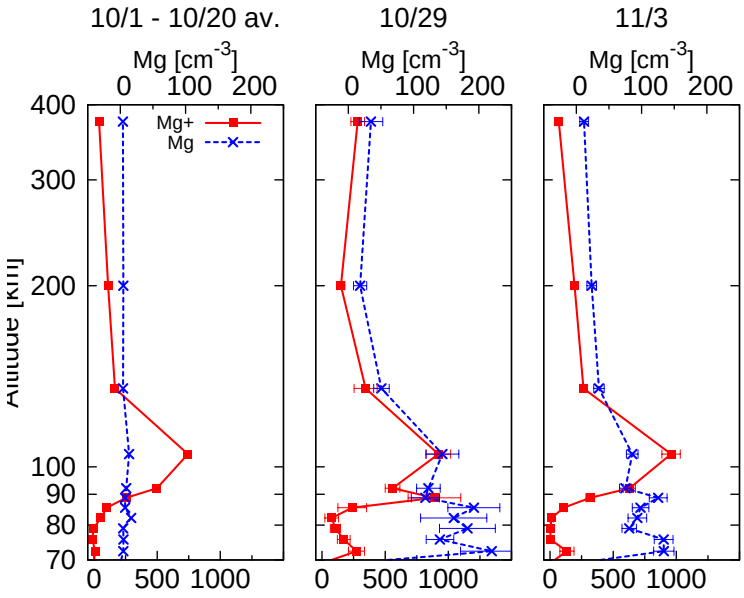

Figure 42: Average vertical profiles of Mg^+ (solid) and Mg (dashed) during October 29, and daily average profiles on October 29 and November 3, **averaged from 90°S – 90°N geographical latitude and all longitudes.** Singly ionized magnesium is only slightly affected at November 3, neutral Mg, however, shows increased number densities at all altitudes. Largest deviations from the average profile of Mg occur below 120 km.

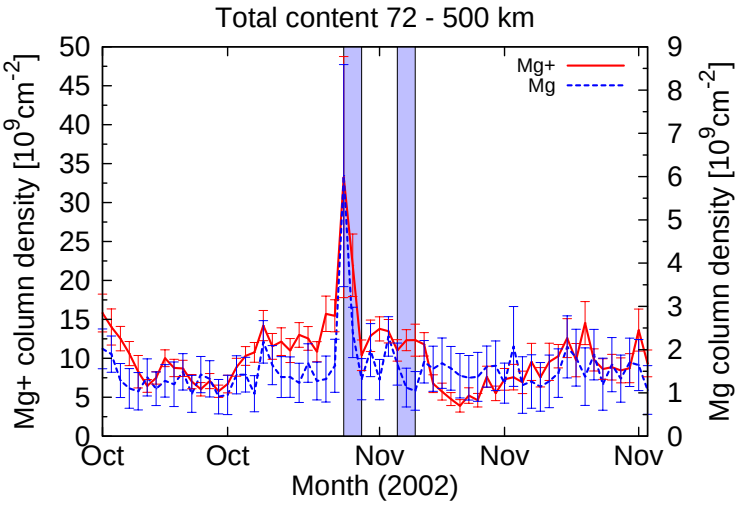

Figure 43: Total column densities of Mg^+ (solid) and Mg (dashed) during October and November 2003 **averaged from 60° to 90° geomagnetic latitude and all longitudes.** Blue strips refer to the first and second SPE under consideration, i.e. the time periods October 28 – 30 respectively November 3 – 5. Maximum proton fluxes occurred on October 29 and November 3–4, see Figure 36. Both magnesium species exhibit a pronounced isolated total content peak abundance on October 28, one day before the maximum of the particle fluxes on October 29. The November 4 event is not visible in the data, the total content does not change significantly during November 3 – 5.

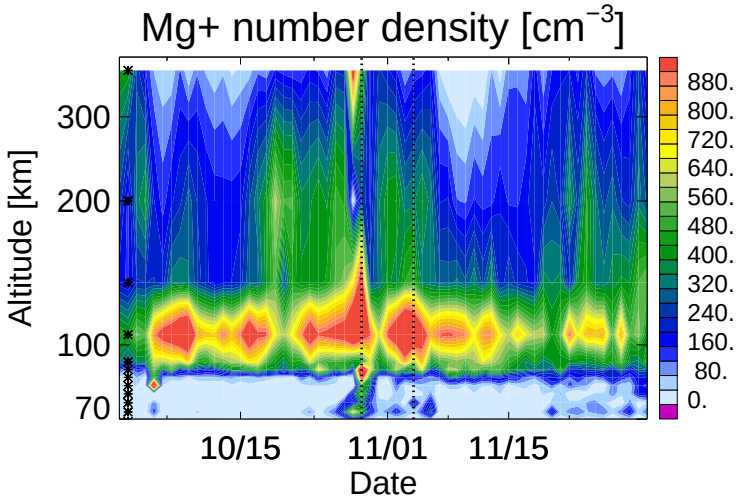

Figure 44: Average vertical distribution of Mg^+ during October and November 2003 **averaged from 90°S – 60°S and 60°N – 90°N geomagnetic latitude and all longitudes.** Asterisks on the left denote the center altitudes of the retrieval pixel grid, see Section 3.3. Increased values of Mg^+ above 150 km are observed during late October, early November and late November. The October 29 event is clearly visible in the data. However, Mg^+ exhibits maximal values around 400 km already on October 28, one day before the maximum of the particle flux (see Figure 36). The October 29 Mg^+ abundance at 400 km is lower than on October 28. Increased values below 120 km occur on October 28 (around 72 km) and October 29 (between 70 and 120 km). On November 3, Mg^+ is increased only at mid altitudes between 120 and 250 km.

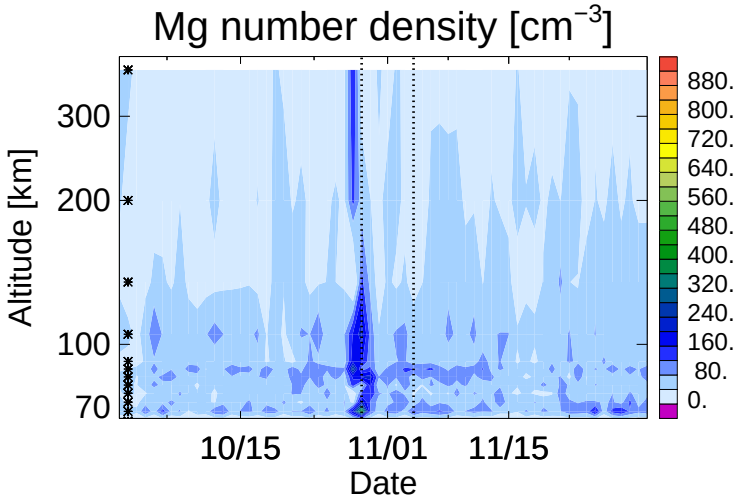

Figure 45: Average vertical distribution of Mg during October and November 2003 **averaged from 90°S – 60°S and 60°N – 90°N geomagnetic latitude and all longitudes.** Asterisks on the left denote the center altitudes of the retrieval pixel grid, see Section 3.3. Mg^+ is significantly increased at altitudes between 70 and 150 km on October 29. Note that highest abundances of Mg around 400 km are present on October 28, as is the case for Mg^+. One day later, the values are back to average again. The November 3/4 event is not visible in the data shown here.

The impact of the November 4 SPE on the profiles as well as on the total content is smaller than that of the October 29 event. It is not clear whether the effects observed on November 4 are a result of the increased proton flux from the Sun. It has to be noted that the spatial as well as temporal variability of both Mg species is quite large.

A possible source of systematic error for all observations presented here is a failed normalization of the radiances I (i.e. usage of a wrong solar spectrum). As described in Section 3, the retrieval measurement input is I/F, where I is the measured radiance and F is the solar flux. If instead of the correct solar spectrum of the respective orbit, any arbitrary spectrum would be used, the retrieval results will be obviously wrong. If a solar spectrum with from a day with smaller MgII index would be used, the retrieval underestimates the true magnesium content. Accordingly, a falsely used spectrum with higher MgII index than in reality would lead to an overestimation of the true atmospheric state. However, this effect would then affect all latitude bands equally. The observations of the 2003 solar proton events in October and November, however, show distinct features in different latitude bands. The strongest variations are observed near the geomagnetic poles, the tropical atmosphere is rather less affected in comparison. It can thus be concluded that the normalization procedure was done correctly and the observed variations in the distribution of the magnesium species are in fact a result of atmospheric processes.

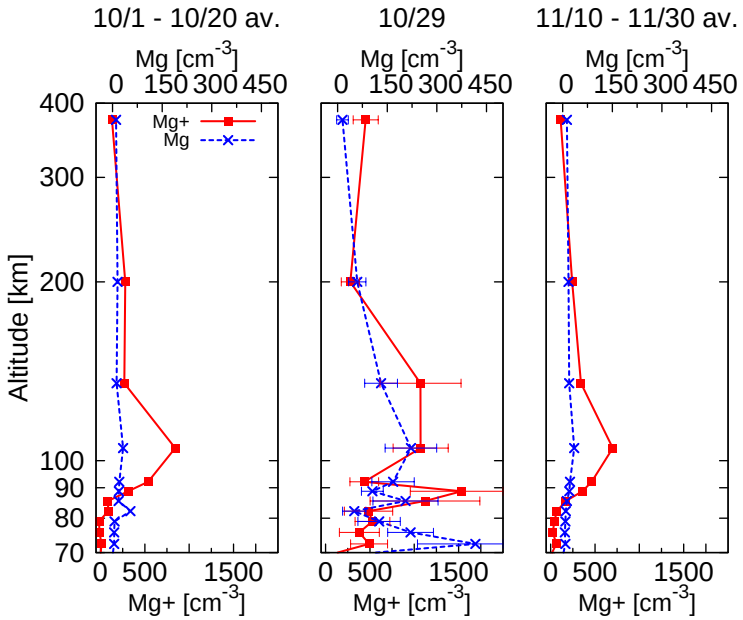

Figure 46: Average vertical profiles of Mg^+ (solid) and Mg (dashed) during October 10 – 20, October 29 and November 10 – 20, **averaged from 90°S – 60°S and 60°N – 90°N geomagnetic latitude and all longitudes.** Significant increases in Mg^+ occur on October 29 at all altitudes except around 200 km. A pronounced layer of Mg^+ is formed at 89 km. This layer is broader compared to all other latitude regions [Scharringhausen, 2007].

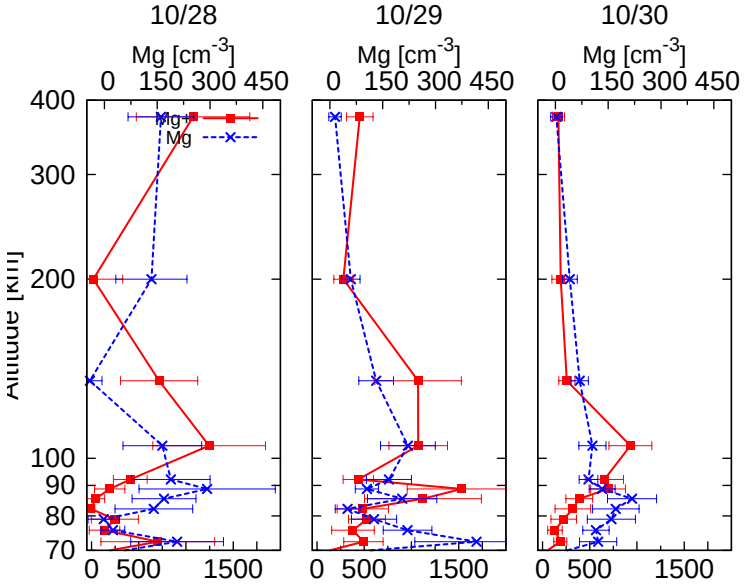

Figure 47: Daily average vertical profiles of Mg^+ (solid) and Mg (dashed) during October 28 – 30, **averaged from 90°S – 60°S and 60°N – 90°N geomagnetic latitude and all longitudes.** As already noted, the Mg^+ layer at 89 km is only observed on October 29. Mg^+ values at high altitudes around 400 km are increased during all three days of the event. Neutral Mg is increased at high altitudes around 400 km during the first two days of the event. On October 20, the Mg^+ abundance at 400 km is at average levels again. Neutral Mg is increased only during the first day of the event. Maximum values of Mg on October 28 are observed between around 89 km. Another layer of high abundance forms at low altitudes around 72 km. On October 29, Mg is maximal at 72 km. On October 30, this low-altitude maximum is not present any more, maximal Mg abundances are now observed at 89 km.

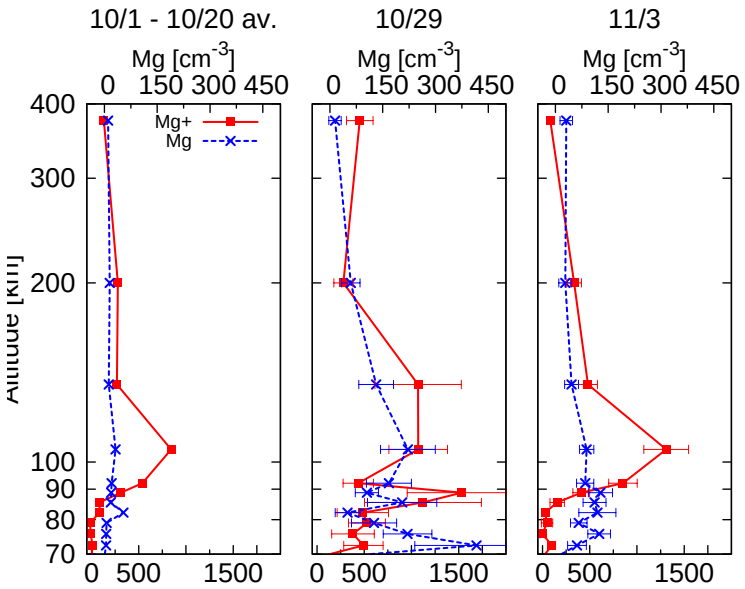

Figure 48: Average vertical profiles of Mg^+ (solid) and Mg (dashed) during October 29, and daily average profiles on October 29 and November 3, **averaged from 90°S – 60°S and 60°N – 90°N geomagnetic latitude and all longitudes.** The Mg^+ profile on November 3 exhibits significantly increased values around 120 km. However, low and high altitudes are not affected. The Mg profile is increased at low altitudes below 120 km. However, absolute values of October 29 exceed the November 3 values by a factor of more than three.

6.2 Discussion

It is reasonable to assume that the ionization rate to form Mg^+ from neutral Mg is increased during solar proton events. As a result of large perturbations in the Earth's magnetosphere and the increased particle impact in particular in polar regions, ionized species are more likely to exhibit high abundances. On the one hand, direct ionization due to particle impact to form Mg^+ from Mg is possible. On the other hand, charge transfer is increased.

As pointed out by Jackman et al. [2005], the October 2003 SPE led to largely increased production of odd nitrogen (NO_y). This production is a result of dissociation of nitrogen molecules and subsequent reaction with oxygen to form odd nitrogen species such as NO. At mesospheric altitudes, this NO is readily ionized either by photo-ionization or particle impact to form NO^+. This species is an important reaction partner for Mg to form Mg^+ by charge transfer (see reaction (1), Section 2).

A possible source for neutral Mg is presented by recombination of Mg^+ with electrons. The observation of higher Mg abundances is thus consistent with the higher concentration of both species during times of high solar proton fluxes. This is probably the source of neutral Mg at high altitudes around 400 km.

Jackman et al. [2005] reported significant losses of mesospheric ozone at altitudes of about 70 km, resulting from increased production of odd hydrogen (HO_x). A longer lasting ozone depletion was attributed to increased NO_y production during the event. A possible reason for the enhancements of neutral Mg at lower altitudes around 70 km is presented by lower ozone number densities, as reaction with ozone destroys neutral Mg (reaction (10), Section 2). It is, however, unlikely that the ozone depletion is the only source of Mg.

Increased release from the reservoir species $Mg(OH)_2$ by reaction with atomic hydrogen is likely to be the main source of neutral Mg at lower altitudes (reactions (14), (15), see Section 2). This is consistent with model calculations that suggest increased OH levels at altitudes around 70 km [Jackman et al., 2005].

The formation of a pronounced Mg^+ layer at an altitude of 89 km exclusively on October 29 is restricted to mid and high latitudes and most pronounced in regions of high geomagnetic latitude (see vertical profiles as shown in Figure 46). It is noteworthy that a simultaneously occurring corresponding layer in the neutral Mg is not observed. Nor is Mg significantly depleted. Thus, a temporally and spatially restricted conversion of the neutral into the ionized species can be excluded. Model calculations carried out by Plane and Helmer [1995] and Fritzenwallner and Kopp [1998] suggested a layer of MgO^+ between 85 and 90 km (see Figure 2, Section 2). A possible source of neutral Mg (which is rapidly ionized at within this altitude range) associated with the solar proton event is presented by the following reactions:

$$MgO^+ + e^- \rightarrow Mg + O \quad (26)$$

$$MgO^+ + O \rightarrow Mg^+ + O_2 \quad (27)$$

However, the peak abundance of MgO^+ within the layer was calculated to be just 10 cm^{-3} in times of average solar activity (neither Plane and Helmer [1995] nor Fritzenwallner and Kopp [1998] assume any particular solar conditions), i.e. even a complete conversion from MgO^+ to Mg^+ could not yield the observed

peak concentration of 1000 – 1500 cm^{-3} . An increased production of MgO^+ to satisfy the increased Mg^+ abundance through reactions (26) and (29) may be resulting from reaction of Mg^+ with molecular oxygen and subsequent reaction with atomic O (which is increased during the solar proton event):

$$Mg^+ + O_2 + N_2 \rightarrow MgO_2^+ + N_2 \quad (28)$$

$$MgO_2^+ + O \rightarrow MgO^+ + O_2 \quad (29)$$

However, reaction (28) obviously depletes Mg^+. Thus, no conclusion can be given. It is desirable to carry out a more thorough model study including the mesospheric and thermospheric conditions during a solar proton event and the according particle fluxes into the Earth's atmosphere. A direct measurement of a number of molecular magnesium species (see Section 2) will certainly be the ideal way.

What remains unclear is the fact that tropical Mg^+ and Mg is increased at all. The direct particle impact can be assumed to be negligible, as solar particles are deflected by the Earth's magnetic field towards to poles. A similar argument holds for the mid-latitudes regions. The zonally averaged cross sections for tropical regions and mid-latitudes show increased number densities of Mg^+ at high altitudes shortly after the first event on October 29 ([Scharringhausen, 2007]).

The Polar regions, however, exhibit maximal number densities at high altitudes just on October 29, whereas the regions of high geomagnetic latitude (Figures 44, 45) exhibit increased high-altitude number densities already one on October 28. Note that the abundance of neutral Mg at high altitudes shows a behaviour similar to that of Mg^+ in polar regions (both geographical and geomagnetic), whereas the high-altitude abundance of neutral magnesium in the tropics and mid-latitudes is not affected during either event.

This observations give rise to the assumption that Mg^+ as well as neutral Mg is produced at high-latitude regions during the October 29 event. A significantly increased flux of energetic particles may has arrived at the Earth even on October 28. If the energies of these particles are below 0.8 MeV, they are not observed by the GOES instrument (see Figure 36). The ionized species is then transported towards lower latitudes. This cannot be accomplished by neutral winds, as these would drive the neutral species as well. Additionally, the number density above 120 km is too low and thus the ion-neutral collision frequency is quite small. The motion of ionic species is thus dominated by interactions of the ionized particles with the E and the B fields. The transport of the ions is possible through gyro motion around the magnetic field lines similar to electrons and protons in the Van-Allen belts.

It should be noted that the results of this section do not contradict the findings presented in Section 5.1 as the solar outburst of October/November 2003 has introduced particles of much higher energy into the atmosphere than the average solar flux respectively variations of same.

7 Magnesium species and meteor activity

The meteoric influx is not constant throughout the year. In fact, there are a number of *meteor showers* the Earth encounters on a regular basis. These

showers results from the passage through the trail of a comet as both the Earth and the comet are orbiting the Sun. A number of comets are returning regularly, and these may in turn cause regularly returning meteor showers. The strength of such a shower is then measured by the *Zenithly Hourly Rate*. This value gives the number of meteors that would be observed under ideal conditions (i.e. clear sky, no clouds) if the shower would originate in zenith. The actual count rate depends on the flight direction of the shower as well as on the observer's field-of-view and viewing direction. However, the ZHR is a suitable means to compare the relative strengths of different meteor showers. The strongest regularly returning showers exhibit ZHRs of 100 – 120.

As is it generally believed that meteoric influx of cosmic dust is the major source of mesospheric and thermospheric metal species (compare Section 1), it is suggestive to expect that the total abundance of metal species is correlated with the meteoric influx. In particular, periods of high meteoric activity should result in correspondingly higher values of the total columns of Mg and Mg^+.

In this section, the five strongest regularly returning meteor showers are considered and their impact on the Mg^+ and Mg content is investigated. Table 4 gives a review of these showers. Each shower is characterized by its activity period, its day of maximal activity and the corresponding ZHR value.

To investigate the impact of meteoric showers on the Mg^+ and Mg content, daily average values in periods of high meteoric activity are compared to values in times of low activity. The period of highest meteoric influx is mid November through mid January, as three meteoric showers of high ZHR occur. Note that the strength of the Leonid shower is highly variable. The respective ZHR varies from 20 to 120, depending on the particular year (compare Table 4).

Shower	Activity period	Maximum	ZHR	Associated comet
Quadrantids	Jan 1 – Jan 5	Jan 3	120	C/1490 Y1
η-Aquarids	Apr 19 – May 28	May 5	60	Halley's comet
Perseids	Jul 17 – Aug 24	Aug 12	100	Swift-Tuttle
Leonids	Nov 14 – Nov 21	Nov 17	$\leq$120(*)	Temple-Tuttle
Geminids	Dec 7 – Dec 17	Dec 14	120	3200 Phaeton

Table 4: Review of prominent periodically returning major meteor showers. The ZHR value denotes the *Zenithal Hourly Rate*, i.e. the number of meteors that can be seen under clear, dark sky conditions and the shower assumed to come from zenith direction. The actual meteor count depends on the flight direction of the shower and the viewing direction of the observer. The ZHR is an upper estimate, but can be conveniently used to compare the strengths of different showers. Note that the activity periods do not exceed one week. The ZHR of the Leonids (*) varies from year to year (e.g. 2006: ZHR = 100). The given value is a lower estimate.

7.1 Observations

This section presents a case study of the impact of meteoric activity on the total content of both magnesium species. As an illustrative example, the year 2006 is considered. See Scharringhausen [2007] for a detailed view on all six years of SCIAMACHY measurements.

Figures 49 and 50 show the globally daily averaged total content of Mg^+ and Mg. Major meteor showers as listed in Table 4 are marked in light green, the day of maximal activity is marked dark green.

The following list presents the observations made during the five meteor showers given in Table 4.

- Quadrantids (January 1 – January 5): The 2006 Quadrantids do not affect the magnesium content significantly. This holds for both species.
- η-Aquarids (April 19 – May 28): No trend in neither magnesium species can be observed during the shower.
- Perseids (July 17 – August 24): Total column amounts of Mg^+ exhibit a minimum around August 1 and increase during the second half of the shower. Neutral Mg is constant during the shower with respect to measurement errors.
- Leonids (November 14 – November 21): The ZHR of this year was approximately 110. Values of Mg^+ exhibit a maximum near the day of maximal activity of the 2006 Leonids. During the second half of the shower, values of Mg^+ are decreasing. However, variations during the 2006 Leonids do not exceed the magnitude of 2006 variations in general. The same holds for neutral Mg.
- Geminids (December 7 – December 17): No significant trend in neither Mg species is observed.

7.2 Conclusions

Within the measurement error margins, no significant impact of periods of high meteoric activity on the total content of either Mg species has been observed. The variations during the showers are either not significant or are of the same order of magnitude as variations in periods of low meteoric activity.

Assuming influx of cosmic dust to be the primary source of mesospheric and thermosphere magnesium species, it can be concluded that the additional mass influx brought along with prominent and bright meteor showers is negligible compared to the background flux of cosmic dust into the atmosphere. Variations in both magnesium species have to be explained using other mechanisms.

These results are consistent with findings of former investigations carried out by Fesen and Hays [1982a] and Joiner and Aikin [1996]. While the authors of the first publication report on results of the limb-viewing satellite instrument on the Atmospheric Explorer E satellite, Joiner and Aikin [1996] present results using the GOME nadir-viewing instrument onboard the ERS-2 satellite. However, neither data set suggests a significant impact of meteoric shower activity on the Mg^+ content of the upper atmosphere. In case of Joiner and Aikin [1996], the

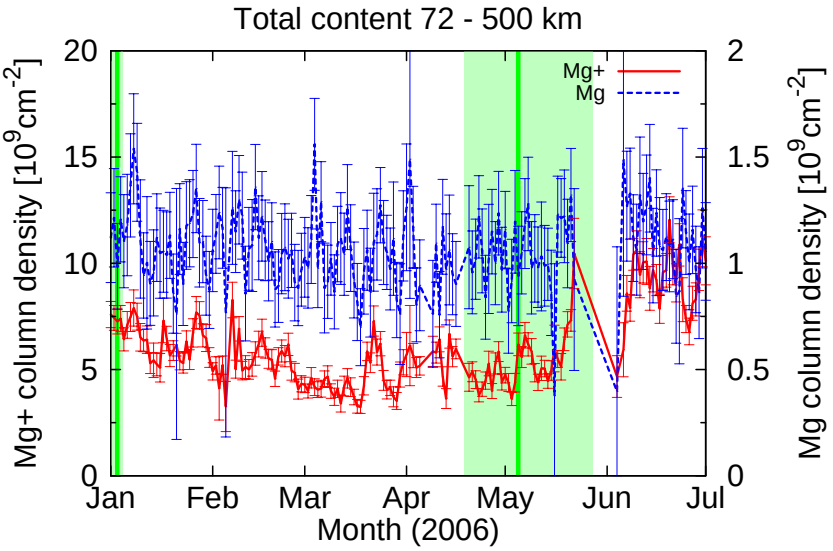

Figure 49: Total content of Mg^+ (solid) and Mg (dashed) during January 2006 – June 2006. Tick marks denote the first day of the month. Green strips denote periods of high meteoric activity, dark green areas refer to days of maximal activity, see Table 4.

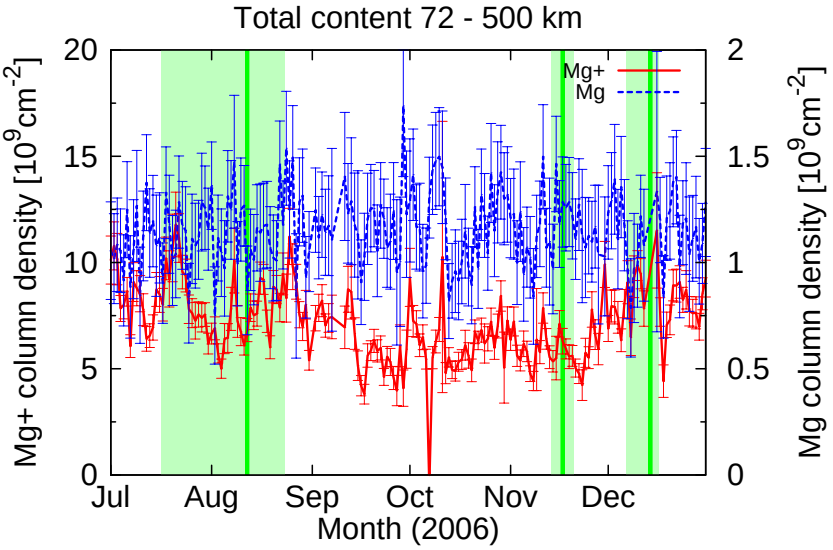

Figure 50: Total content of Mg^+ (solid) and Mg (dashed) during July 2006 – December 2006. Meteor showers are marked, see Figure 49.

analysis extends to the neutral Mg as well, with negative result for all meteor showers under consideration.

8 Estimation of the total influx of cosmic dust from total content and loss rates of Mg

The total influx of meteoric material into the atmosphere is subject to intense research, but still no certain numbers are known. Early radar measurements suggest a total mass flux of approximately 44 t/d [Hughes, 1978]. These estimates have been revised to 80 – 120 t/d. Long exposure measurements based on satellite platform instruments yielded estimates of about 130 t/d [McBride and McDonnell, 1999]. Rather indirect methods are the investigation of stratospheric aerosols and the corresponding content of meteoric iron and investigations or iridium sediments in the Earth's ocean floors. While the first method yielded values of 20 – 100 t/d [Cziczo et al., 2001], the second suggested higher values of 240 t/d [Wasson and Kyte, 1987].

For a steady state, the sources and sinks have to equal. Thus, knowing the fraction of neutral magnesium contained in meteoric material, an estimation of the loss rate in the Earth's atmosphere will yield an estimate of the total mass of meteoric material entering the atmosphere per day. See Section 2 for a detailed description of loss reactions for Mg and Mg^+. Main loss reactions are resulting from reaction with ozone, charge transfer with O_2^+ and NO^+ and photoionization (see reactions (10), (3), (2),(1) in Section 2).

The loss of Mg at an particular altitude h is calculated as the product of the loss rate δL and the number density [Mg]:

$$L(h) = \delta L(h) \cdot [\mathrm{Mg}](h) \tag{30}$$

Multiplication of this value with the area $A(h)$ of the shell at atmospheric level h yields the global loss at altitude h. This value has to be multiplied with 86400 s/d to obtain the loss per cm^{-2} and day. Assuming a constant isotropic influx, the global loss per day is then calculated as

$$\begin{aligned} L^* &= 86400 \cdot \int_{H_0}^{H_1} \delta L(h) \cdot [\mathrm{Mg}](h) \cdot A(h)\, dh \\ &\approx 86400 \cdot A_0 \cdot \int_{H_0}^{H_1} \delta L(h) \cdot [\mathrm{Mg}](h)\, dh. \end{aligned} \tag{31}$$

Here, A_0 denotes the surface area of the atmospheric shell at level 120 km. The second equation is a good approximation of the first, since the surface areas of the atmospheric shells at 0 and 120 km differ only by 3%. Thus, $A(h)$ can be considered constant. Integration over altitude is performed between $H_0 = 70$ km and $H_1 = 120$ km. This choice is reasonable as the measurements do not extend to lower altitudes and on average no significant Mg abundance has been measured above 120 km. Reading the values from Figure 26 on page 36, using an average vertical profile of Mg as given in Section 4.1.1 and inserting all these quantities in equation (31), a global influx of 927 kg/d of neutral Mg is estimated.

It can be assumed that the magnesium in meteoric material is not ionized. The average mass fraction of Mg in cosmic dust has been reported by Hughes [1978] to be approximately 13%. Assuming that the total meteoric content of MG is ablated and transferred into the gas phase, a total influx of approximately 7130 kg/d would result. However, McNeil et al. [1998] noted that contrary to sodium, magnesium and calcium may not ablate completely from the dust particle. A differential ablation model accounting for individual ablation altitudes and different particle sizes and entry velocities was applied to estimate the deposition of meteoric material in the upper atmosphere. The results provided strong evidence that the fraction of metal species that do not ablate completely from the dust particle depends primarily on the entry velocity of the particle. This velocity is not constant throughout the total particle population. Higher velocities result in a more complete ablation of magnesium and other meteoric metals from the dust particles. At approximately 30 km/s, the complete content of sodium, magnesium and calcium is ablated from the particle [McNeil et al., 1998], whereas e.g. 14 km/s leaves half of the metallic content of calcium and magnesium in the particle.

A number of velocity distributions have been tested by McNeil et al. [1998], and the resulting metal profiles have been compared with measured values. However, the resulting picture is far from being homogeneous. Best matches with measured column density ratios of Na/Ca, Na^+/Ca^+ and Mg^+/Na^+ have been obtained assuming a population of fast particles with entry velocity 60 km/s and another larger population of slow particles with 11 km/s. The latter particles are assumed to make up 98% of the total particle amount. This velocity distribution results in 87% residual amount (not ablated) of magnesium in the dust particles. Using 927 kg/d of ablated magnesium input into the atmosphere, 55 t/d of meteoric material have to enter the atmosphere every day. This is well within the range of earlier estimates.

It should be noted that 11 km/s is the lowest possible velocity for a dust particle to enter the atmosphere, as this is just the minimal velocity for escape from the Earth's potential well. A dust particle originating at an infinite distance would therefore enter the atmosphere with approximately the escape velocity.

However, the origin of meteoric dust is still not clear. McDonnell [1980] suggested that the Earth is surrounded by a cloud of cosmic dust of mainly asteroidal origin. This cloud is stationary within the solar system and particles leave the cloud and hit the Earth as a result of gravitational or other perturbations. Another possible origin of cosmic dust, however, are regular or irregular cometary objects. These objects enter the solar system with higher velocities. The maximum velocity for an regularly returning object on an parabolic (i.e. circular or elliptical) orbit is 72 km/s at 1 astronomical unit.

It can be concluded that the velocity distribution of cosmic dust particles significantly impacts the amount of ablated material and that this distribution is still not known to a good extend. Thus, the best estimate to do is assuming the majority of comic dust entering the atmosphere at the smallest possible velocity of 11 km/s. This yields an lower estimate of the meteoric influx of 55 t/d.

It should be noted that this mass influx is negligible compared to the total mass of Earth of $5.97 \cdot 10^{21}$ t. Assuming that the Earth of approximately 5 billion years old and that during this time the influx of meteoric material has not changed, a total mass of 10^{14} t has been added to the Earth's mass. This

is more than seven orders of magnitude below the mass of Earth and thus negligible.

References

A. C. Aikin and R. D. McPeters. Meteoric material and the behavior of upper stratospheric polar zone. *Geophysical Research Letters*, 13:1300–1303, November 1986.

A. C. Aikin, M. L. Chanin, J. Nash, and D. J. Kendig. Temperature trends in the lower mesosphere. *Geophysical Research Letters*, 18:416–419, March 1991.

Aikin, A. C., Grebowsky, J. M. and Burrows, J. P., 2004: Satellite measurements of the atmospheric content of metallic ion and neutral species. *Advances in Space Research*, **33**, 1481–1485.

Anderson, J. G. and Barth, C. A., 1971: Rocket Investigation of the MgI and MgII Dayglow. *Journal of Geophysical Research*, **76**, 16, 3723–3731.

Bilitza, D., 2001: International Reference Ionosphere 2000. *Radio Science*, **36**, 2, 261–275.

Brasseur, G. P. and Solomon, S., 1984: *Aeronomy of the Middle Atmosphere: Chemistry and Physics of the Stratosphere and Mesosphere*. third edn., Kluwer Academic Publishers.

J. Correira, A. C. Aikin, J. M. Grebowsky, and J. P. Burrows. Spatial and temporal enhancements of meteoritic metal ions in the upper atmosphere. *AGU Fall Meeting Abstracts*, pages A4+, December 2005.

Covington, A. E., 1969: Solar Radio Emission at 10.7 cm, 1947-1968. *Journal of the Royal Astronomical Society of Canada*, **63**, 125.

D. J. Cziczo, D. S. Thomson, and D. M. Murphy. Ablation, flux, and atmospheric implications of meteors inferred from stratospheric aerosol. *Science*, 291:1772–1775, March 2001.

Dominion Radio Observatory, Penticton, Canada, 2007: Solar Radio Monitoring Programme. `http://www.drao-ofr.hia-iha.nrc-cnrc.gc.ca/icarus/www/sol_home.shtml`.

C. G. Fesen and P. B. Hays. Mg^+ morphology from visual airglow experiment observations. *Journal of Geophysical Research*, 87(A11):9217–9223, 1982.

Fesen, C. G. and Hays, P. B., 1982b: Two-dimensional inversion technique for satellite airglow data. *Applied Optics*, 21, 20, 37843791.

Fesen, C. G., Hays, P. B., and Anderson, D. N., 1983: Theoretical Modeling of Low-Latitude Mg^+. *Journal of Geophysical Research*, **88**, A4, 3211–3223.

Fritzenwallner, J. Kopp, E., 1998: Model Calculations of the Silicon and Magnesium Chemistry in the Mesosphere and Lower Thermosphere. *Advances in Space Research*, **21**, 6, 859–862.

Gérard, J. C., and Monfils, A., 1978: The MgII Equatorial Airglow Altitude Distribution. *Journal of Geophysical Research*, **83**, A9, 4389–4391.

GFZ – Germany's National Research Centre for Geosciences, Potsdam, 2007, `http://www.gfz-potsdam.de/pb2/pb23/niemegk/kp_index/index.html`.

R. A. Goldberg and A. C. Aikin. Comet encke: Meteor metallic ion identification by mass spectrometer. *Science*, 180:294296, April 1973.

Golub, G. H. and v. Loan, C. F., 1996: *Matrix Computations*. third edn., Baltimore and London: The John Hopkins University Press.

Hanson, W. B. and Sterling, D. L., 1972: Source and Idetication of Heavy Ions in the Equatorial F Layer. *Journal of Geophysical Research*, 77, 28, 55305541.

Hedin, A., 1991: Extension of the MSIS Thermosphere Model into the Middle and Lower Atmosphere. *Journal of Geophysical Research*, **96**, 1159.

Horwitz, J. R. and Lockwood, M., 1985: The Cleft Ion Fountain: A Two-Dimensional Kinetic Model. *Journal of Geophysical Research*, **90**, A10, 9749–9762.

J. P. Hughes. *Cosmic Dust*. J.A.M. McDonell, Ed. J. Wiley, first edition, 1978.

D. M. Hunten. An iron deficiency in polar mesospheric clouds. *Sience*, 304: 395396, 2004.

Jackman, C. H., DeLand, M. T., Labow, G. J., Fleming, E. L., Weisenstein, D. K., Ko, M. K. W., Sinnhuber, M. and Russell, J. M., 2005: Neutral atmospheric influences of solar proton events in October–November 2003. *Journal of Geophysical Research*, **110**.

J. Joiner and A. C. Aikin. Temporal and spatial variations of upper atmosphere mg. *Journal of Geophysical Research*, 101:5239–5250, 1996.

Kaiser, J., 2001: *Atmospheric Parameter Retrieval from UV–Visible–NIR Limb Scattering Measurements*, University of Bremen, Institute of Environmental Physics.

O. Kalashnikova, M. Horanyi, G. E. Thomas, and O. B. Toon. Meteoric smoke production in the atmosphere. *Geophysical Research Letters*, 27:32933296, October 2000. doi: 10.1029/1999GL011338.

Lockwood, M., Horwitz, J. R., Chandler, M. O., Waite, J. H., Moore, T. E. and Chappell, C. R., 1985: The Cleft Ion Fountain. *Journal of Geophysical Research*, **90**, A10, 9736–9748.

Moore, T. E., Lockwood, M., Chandler, M. O., Waite, J. H., Chappell, C. R., Persoon, A. and Sugiura, M., 1986: Upwelling O^+ Ion Source Characteristics. *Journal of Geophysical Research*, **91**, A6, 7019–7031.

N. McBride and J. a. m. McDonnell. Meteoroid impacts on spacecraft:sporadics, streams, and the 1999 leonids. *Planetary and Space Science*, 47:1005–1013, August 1999.

J. A. M. McDonnell. *Mircoparticle studies by space instrumentation (in* Cosmic Dust*)*. John Wiley, New York, first edition, 1980.

W. J. McNeil, T. L. Shu, and E. Murad. Differential ablation of cosmic dust and implications for the relative abundances of atmospheric metals. *Journal of Geophysical Research*, 103(D9):10,899–10,911, 1998.

Minschwaner, K., Shukla, N., Fortna, C., Budzien, S., Dymond, K., and McCoy, R., 2004: Observations of Ultraviolet Emission from Mg^+ in the Lower and Middle Thermosphere. *AGU Fall Meeting 2004, Poster presentation*, **SA21A-0337**.

E. Murad,W. Swider, and S. W. Benson. Possible role for metals in stratospheric chlorine chemistry. *Nature*, 289:273, January 1981.

D. M. Murphy, D. S. Thomson, and M. J. Mahoney. In situ measurements of organics, meteoritic material, mercury, and other elements in aerosols at 5 to 19 kilometers. *Science*, 282:1664, November 1998.

NASA Goddard Space Flight Center, N., 2007b: NASA Goddard Modelweb Online resource. `http://modelweb.gsfc.nasa.gov/models/msis.html`.

NASA Goddard Space Flight Center, N., 2007a: NASA Goddard Modelweb Online resource. `http://modelweb.gsfc.nasa.gov/models/iri.html`.

NIST, 2005: National Institute of Standards and Technology: Atomic Spectra Database. `http://physics.nist.gov/PhysRefData/ASD/lines_form.html`.

NOAA/National Weather Service, 2007: Solar and Geomagnetic Indices. `http://www.sec.noaa.gov/Data/index.html#indices`.

Plane, J. M. C., and Helmer, M., 1995: Laboratory Study of the Reactions Mg + O_3 and MgO + O_3, Implications for the Chemistry of Magnesium in the Upper Atmosphere. *Faraday Discussions*, **100**, 411–430.

Plane, J. M. C., 2003: Atmospheric Chemistry of Meteoric Metals. *Chemical Reviews*, **103**, 2003, 4963–4984.

J. M. C. Plane, B. J. Murray, X. Chu, and C. S. Gardner. Removal of meteoric iron on polar mesospheric clouds. *Science*, 304:426428, 2004.

F. Lübken and J. Höfner. Experimental evidence for ice particle interaction with metal atoms at the high latitude summer mesopause region. *Geophysical Research Letters*, 31(L08103), 2004.

Roddy, P. A., Earle, G. D., Swenson, C. M., Carlson, C. G. and Bullett, T. W., 2004: Relative concentrations of molecular and metallic ions in midlatitude intermediate and sporadic E–layers. *Geophysical Reseach Letters*, **31**.

Rozanov, A., 2001: *Modeling of radiative transfer through a spherical planetary atmosphere*, University of Bremen, Institute of Environmental Physics.

v. Savigny, C., Bramstedt, B., Noel, S., Sinnhuber, M. and Taha, G., 2006: *Comparison of SCIAMACHY pointing retrievals in limb and Occultation geometry*. TN–IUP/IFE–2006–cvs–03, University of Bremen, Intitute of Environmental Physics.

v. Savigny, C., Kaiser, J. W., Bovensmann, H., Burrows, J. P., McDermid, I. S. and Leblanc, T., 2005: Spatial and temporal characterization of SCIAMACHY limb pointing errors during the first three years of the mission. *Atmospheric Chemistry and Physics*, **5**, 2593–2602.

M. Scharringhausen. *Investigation of mesospheric and thermospheric magnesium species from space*. PhD thesis, University of Bremen, Institute of Environmental Physics, 2007.

Schmahl, E. J. and Kundu, M. R., 1994: Solar cycle variation of the microwave spectrum and total irradiance. *Solar Physics*, **152**, 167–173.

M. E. Summers and D. E. Siskind. Surface recombination of O and H2 on meteoric dust as a source of mesospheric water vapor. *Geophysical Research Letters*, 26:18371840, July 1999. doi: 10.1029/1999GL900430.

Tapping, K. and Murdin, P., 2000: Solar Activity Indices. *Encyclopedia of Astronomy and Astrophysics*.

J. T. Wasson and F. T. Kyte. Comment on the letter 'on the influx of small comets into the earth's atmosphere. ii - interpretation'. *Geophysical Research Letters*, 14:779–+, 1987.